PONTIFICIA UNIVERSIDAD CATOLICA DE CHILE

ESCUELA DE INGENIERIA

ENHANCEMENT OF THE COOLING CAPABILITY OF A CPV SYSTEM USING MICROCHANNEL HEAT SINK WITH TRIANGULAR RIBS

MARIO DI CAPUA HIDALGO

Thesis submitted to the Office of Research and Graduate Studies in partial fulfillment of the requirements for the Degree of Master of Science in Engineering

Advisor:

AMADOR GUZMÁN

RODRIGO ESCOBAR

Santiago de Chile, (January, 2018)

PONTIFICIA UNIVERSIDAD CATOLICA DE CHILE

ESCUELA DE INGENIERIA

ENHANCEMENT OF THE COOLING CAPABILITY OF A CPV SY|STEM USING MICROCHANNEL HEAT SINK WITH TRIANGULAR RIBS

MARIO DI CAPUA HIDALGO

Members of the Committee:

RODRIGO ESCOBAR M.

AMADOR GUZMAN C.

WOLFRAM JAHN V.A.

ANDRES DIAZ A.

SERGIO MATURANA V.

Thesis submitted to the Office of Research and Graduate Studies in partial fulfillment of the requirements for the Degree of Master of Science in Engineering

Santiago de Chile, (January,2018)

To my family, friends and God. Their support and love have been momentous in my life.

ACKNOWLEDMENT

First of all, I would like to thanks my family and friends for their unconditional love and support. My mother has been momentous with her love and patience to achieve my dreams, as well as my father who gave all for his family and always believed on my capacities. Thanks, mom and dad for giving me your greatest and unconditional love, without you nothing would be possible. In the same way, I would like to thanks my sisters, their love and support have been always important in my life. My beautiful nieces, Isabella and Julieta, their beauty, happiness, and innocence have been the most beautiful thing that I ever had, please never grow up. In the same light, my brothers in law, they have been important with their love and continued support to reach my goals.

I would like to thanks my supervisors, Mr. Amador Guzmán and Mr. Rodrigo Escobar, whom believed in my capacities and the opportunity of working with them.

I want to thanks my friend Andres Arevalo. I have beautiful memories of him and I am completely sure that we will share soon. In the same way, I want to express my gratitude and love to Armando, Redlich, and Mau. With them I overcame the hardest days. Additionally, I would like to thank Valentina Ramirez, who was an important part of my life for the completion of this work. She was my partner, confident, and my support for long time in this endeavor.

Finally, I would like to express my love and faith in God. Thanks for protecting my family and your love always has been with me.

GENERAL INDEX

TABLE INDEX

Pag.

FIGURE INDEX

Pag.

RESUMEN

Simulaciones numéricas fueron desarrolladas para investigar un dispositivo de disipación de calor de microcanal, como opción de enfriamiento para sistemas fotovoltaicos de alta concentración. El software COMSOL 5.1 fue utilizado para resolver las ecuaciones tridimensionales, que consideran disipaciones viscosas y propiedades dependientes de la temperatura. Este estudio propone la integración de los microcanales como parte integral de la estructura de la célula solar, considerando ranuras triangulares como elementos disruptores de capa limite, los cuales buscan a mejorar la transferencia de calor en los microcanales. Las ranuras triangulares se analizan en una distribución alineada y desplazada a lo largo de los microcanales. Además, se desarrolla un análisis numérico para un disipador de calor pasivo, específicamente, una placa plana integrada al sistema fotovoltaico, para establecer un análisis comparativo entre ambos métodos de refrigeración. Los resultados numéricos muestran que un dispositivo de disipación de calor de microcanal puede mantener en un rango muy bajo la temperatura de la celda solar (<301 K). Las ranuras triangulares instaladas en las paredes laterales mejoran la capacidad de transferencia de calor. Los microcanales con ranuras alineados y desplazados aumentan el número de Nusselt entre 1.8 y 1.6 veces, así como también, el factor de fricción promedio entre 3.9 y 2.3 veces, respectivamente, en comparación con el microcanal liso. El dispositivo de disipación de calor de microcanal con ranuras triangulares tiende a ser más eficiente y efectivo a Re≤200, ya que la potencia de bombeo alcanza un alto porcentaje de la potencia total generada por la célula solar cuando Re> 200. Un disipador de calor de microcanal se presenta como una opción más efectiva que un disipador de calor pasivo de placa plana como sistema de refrigeración para un sistema fotovoltaico de alta concentración. Además, la posibilidad de una integración directa del disipador de calor de microcanales en la estructura de la célula solar, la convierte en una opción interesante para aumentar de manera factible la dinámica térmica en un nivel considerable.

Palabras claves: Concentración fotovoltaica, Celda solar de múltiples uniones; Disipador de calor de microcanal.

ABSTRACT

Numerical simulations have been carried out to investigate a Micro-Channel Heat Sink Device as cooling option for a High Concentration Photovoltaic System. The software COMSOL 5.1 was used to solve the three-dimensional equations which consider conjugate heat transfer and viscous dissipations. This study proposes the integration of a microchannel heat sink with forward triangular ribs mounted on the inner sidewalls of the channel as disruptive boundary layer elements. In addition, a numerical analysis was developed to a high concentration photovoltaic system refrigerated by a passive cooling heat sink, to stablish a comparative assessment of the solar cell temperature between both cooling methods. The numerical results show that a microchannel heat sink device can keep in a very low range the solar cell temperature (<301 K). Forward triangular ribs installed on the sidewalls enhance the heat transfer capability. Microchannel with aligned and offset ribs distribution increase the Nusselt number between 1.8 and 1.6 times and increase as well the average friction factors between 3.9 and 2.3 times, respectively, compared to smooth microchannel. Microchannel heat sink device with forward triangular ribs tends to be more efficient and effective at Re≤200, since the pumping power reaches a high percentage of the total power generated by the solar cell when Re>200. At Re=400 the pumping power reaches 41% and 23% of the total power generated by the multi-junction solar cell in the aligned and offset ribs distribution, respectively. The pumping power is greatly reduced when using smooth microchannel, as the maximum pumping power is just 9.5% of the solar cell power at Re=400, however, the resulting solar cell temperature is slightly higher compared to microchannels with aligned and offset ribs configurations. A microchannel heat sink device arises as more effective option than a passive flat plate heat sink as cooling system for a high concentration photovoltaic system. In addition the possibility of a direct integration of micro-channel heat sink into the solar cell structure as is proposed by this study, makes it an interesting option to feasibly increase thermal dynamics in a considerable level

Keywords: Concentrated Photovoltaic; Multi-junction solar cell; Microchannel heat sink.

NOMENCLATURE.

- A: Area (m2).
- Cp: Specific heat $(J/kg * K)$
- Dh: Hydraulic diameter.
- DNI: Direct Normal Radiation (W/m^2)
- Eg: Bandgap Energy.
- Err%: Percentage relative error.
- f: Friction coefficient.
- Fc or CF: Concentration factor.
- H: Height domain (um).
- h_{conv}: Convection coefficient.
- Kn: Knudsen number.
- k: Thermal conductivity $(W/K * m)$.
- L: Length domain (um).
- Nu: Nusselt number.
- P: Power (W).
- ΔP: Pressure drop (kPa).
- p: Pressure. (kPa)
- q_{solar}: Solar energy (W/m^2)
- q_{heat}: Heat flux (W/m^2)
- Re: Reynolds number.
- Rth: Global Thermal Resistance.
- T: Temperature (K).
- U: Velocity (m/s).
- V: Voltage (V).
- W: Width domain (um)
- Wp: Pumping power.

Greek letter

- η_{cell}: Solar cell efficiency.
- λ: Mean free path or wavelength.
- μ: Dynamic viscosity.
- Φ: Viscous dissipation
- ϕ_N^e: Galerkin test fuction.
- ψ_N^e: Diffusion test function

INTRODUCTION

A new generation of PV technology has raised known as multi-junction solar cells, which are multiple p–n junctions made of different semiconductor materials. Multi-junction solar cells are used in high concentrator photovoltaic system (HCPV), where lens and mirrors are used to concentrate the sunlight onto the solar cell, which allows to reduce the use of semiconductor materials, and the area required to generate the same output power [1]. As only a fraction of the solar radiation can be converted into electrical power, the action of concentrating and increasing the amount of solar energy onto a multi-junction solar cell produces an overheating of the solar cell temperature, which is traduced in negative effects in the conversion efficiency and solar cell durability. Kinsey [2] has mentioned that for every °C increase of the cell temperature, the efficiency of the solar cell decreases 0.05%. The overheating implies a reduction of the conversion efficiency, which has as result an increment of the heat generated by the solar cell, therefore a higher overheating. In addition, the increment of the cell temperature accelerate the degradation of the solar cell, as well as the rising temperature will also result in mechanical impact on the solar cell such as deformation on the cell surface, delamination of the transparent layer, and development of micro-cracks on the cell. This is due to different thermal expansion coefficients of several different materials are used to compose the cell structure [3]. Royne [4] concluded that temperature is always the limiting factor for concentration solar cells. Different techniques have been studied and evaluated to handle the overheating of multi-junction solar cell subjected to high concentration. Passive cooling techniques has been proved able to handle the overheating, because its large surface available for heat transfer and since does not demand electrical or mechanical energy input to operate [4]. On the other hand, active cooling system are more effective at high concentration levels, where Royne [4] and Radwan [5,6] highlight microchannel heat sinks as a great option to refrigerate multi-junction solar cells subjected to high solar concentration, because its high thermal performance in small area and the possibility of being incorporated in the solar cell manufacturing process. In addition, the cooling system integrated to a HCPV should be designed considered technical and economic aspects [7], such as: (1) cost of heat sink material drooped increasing the thermal efficiency; (2) concentrator factor; (3) weight that the cooling system adds to the tracker; (4) concentration of radiation implies the miniaturization of the solar cell. Royne [4] mentions that mesoscale cooling devices may not be able to remove great among of heat from small surfaces and micro-technology can assure faster performance, requiring less space, material, and lightweight option.

From the work developed by Tuckerman and Pease [8], microchannel heat sink has raised as great solution as refrigeration system in micro-scale applications, because its ability to remove a large amount of heat from a small area. Microchannels principally have been investigated as refrigeration cooling device for electronic applications, because the continuous miniaturization of electronic components. Few studies have investigated the use of microchannel heat sink in HCPV. Recently, Radwan & Ahmed [9] carried out an analysis that evaluated the influence of microchannel heat sink configuration on the performance of low concentrator photovoltaic system. They concluded that microchannels are an effective method for concentration ratios up to 20, as well as parallel flow microchannel heat sink achieves the highest cell net power. Radwan [10] developed an investigation that analyzed and simulated 2-dimensional model of low concentrating photovoltaic system with smooth microchannel heat sink of 100 μm of height. The study evaluated the influence of operating conditions such as concentration ratio, cooling mass flow rate, wind speed, and ambient temperature. They found that microchannel generates a significant reduction in cell temperature with uniform temperature distribution, and also when Re=100 and CR= 20, the solar cell temperature varies between 306 and 309 K. Other investigation of a microchannel heat sink employed in a HCPV system was carried out by Rahimi [11], where they studied the performance of microchannel and photovoltaic module as a hybrid PV/T system using water as a coolant. They reported that conversion efficiency increased by approximately 30% compared to uncooled conditions. Reddy [12] developed a numerical investigation of microchannel heat sink for solar CPV system, he evaluated different width and aspect ratio of the microchannel. They concluded, based on numerical simulation, that optimum dimensions of the microchannel were 500 μm width and aspect ratio of 8. Moreover, the pressure drop was found to be low in straight flow channels. Ramos-Alvarado [13] calculated the pressure loss and temperature uniformity of the heated walls of different proposed microchannel configurations. They suggested a new design, achieving a smaller pressure drop and better flow and temperature uniformity. They recommended using microchannel distributers for cooling the concentrated PV cells, fuel cells, and electronics. Agrawal [14] developed a 1-dimension thermal model. Concluding that the electrical and thermal 5efficiency of the multichannel PV/T system were higher than those of the single channel PV/T system. Kermani [15] fabricated and investigated a manifold microchannel heat sink for cooling concentrator photovoltaic system with CF=

1000 suns. The heat sink distributed the coolant into alternate inlet and outlet channels in a direction normal to it, thus resulting in a greater heat transfer dissipation rate because of lower pressure drop across the surface to be cooled. W. Chong [16] carried out a performance analysis of a water-cooled multiple-channel heat sinks for ultra-high concentrator photovoltaic system. They proved that with a concentration level of 1800 suns the conversion efficiency achieved was 31.8% for the microchannel heat sink designed.

With respect to the performance of microchannel heat sinks, a large number of investigations have been developed. The tiny size of channel introduces high convection coefficients even for laminar flow regimen, which is the predominated regimen analyzed. The rectangular smooth microchannel has been the basic geometric configuration evaluated from the work of reference [8] and validated with analytic expression, however, in the smooth microchannel hotter fluid accumulates at the channel wall and cooler fluid along the channel core due to continuous growth of the thermal boundary layer. Therefore, most of the early studies carried out seek to enhance the thermal performance of smooth rectangular microchannel evaluating different aspect ratio, channel length, and wall thickness, as well as, other researchers have introduced disruption of boundary layer, and some investigators are evaluated changes in the cross-section shape of microchannel [17]. Disruption of boundary layer has been analyzed incorporating cavities, porous medium, ribs and groove structure, where the heat transfer performance is enhanced because the disruption elements favor to blend hotter and cooler fluid. Ribs have been analyzed in different shapes and configurations inside the channel. L.Chai [18] carried out a parametric investigation based on numerical simulations of the use of fan-shaped ribs with aligned and offset arrangement installed on the inner parallel sidewalls. They reported that for the studied Reynolds range the ribs increase 6 to 101% the average Nusselt number for the aligned configuration, and 4% to 103% increase for the offset arrangement. KC. Cheon [19] developed a numerical simulations of microchannel heat sink with triangular ribs in transverse microchambers. They that found heat transfer rate increases with the increment of rib width and height, but decreases with the increase of rib length. L. Chai [20] extended the work developed by reference [19]. They analyzed numerically different rib shapes in transverse microchambers, where rectangular, backward triangular, diamond, forward triangular and ellipsoidal shapes were analyzed. He reported that ribs in microchambers can effectively prevent the decline of the local heat transfer coefficient and the ellipsoidal ribs in the microchambers shows the best heat transfer performance. L.Chai [21] analyzed through numerical simulations five different rib shapes, including rectangular, backward triangular, isosceles triangular, forward triangular, and semicircular on the inner parallel sidewalls and only considering offset arrangement. They reported that offset ribs result in significant heat transfer enhancement and higher pressure drop, because to the creation of secondary flow, vortexes and boundary layer interruption. This simulation showed that the microchannel with forward triangular offset ribs achieved the highest performance when $Re<350$, on the other hand, when $Re>350$ the semicircular shape presented the highest performance.

The present work evaluates microchannels heat sink with disturbing boundary layer elements with forward triangular shape installed on the parallel inner sidewalls of the channel, as cooling system of a multi-junction solar cell subjected to high concentration level (1000 suns). The forward triangular ribs are analyzed in two configurations along the microchannel: aligned and offset distribution. Offset forward triangular rib distribution was evaluated by L. Chai [21], where they concluded that this rib shape has the highest thermal performance with respect to other rib shapes when Re<350, therefore, forward triangular ribs was selected as the element to enhance the heat transfer performance of microchannels proposed to refrigerate HCPV systems. We carried out CFD simulations using COMSOL 5.1 to analyze in detail the Nusselt number, friction factor, global thermal resistance and pumping power of microchannels with forward triangular ribs compared with a smooth microchannel. Each microchannel domain simulated belong to a heat sink device conformed by 30 parallel microchannels, which is proposed to be integrated on the bottom surface of the solar cell, allowing to reduce considerably the global thermal resistance, the weight of the whole system, and offer a integration (solar cell-heat sink) that can be carry out in the manufacturing process of the HCPV receiver. Based on the data obtained from the microchannel simulations, the temperature and effective solar cell power are determined for different Reynold numbers (100 to 400), enabling to determine if microchannels with ribs are a suitable option as cooling system for HCPV, considering the temperature and effective solar cell power. In addition, simulations of a flat plate heat sink were developed to evaluate the solar cell temperature achieved with this passive cooling system under different surrounding temperature, with the intention to quantify the enhancement on the cooling capability in multi-junction solar cell by using a heat sink conformed by microchannels. This article is conformed as follows: (2) HCPV with passive cooling system; (3) Microchannel heat sink incorporated in a HCPV system; (4)

Microchannel domain and governing equations; (5) Solution methodology and convergence test; (6) Data acquisition; (7) Numerical validation; (8) Results and Discussion; (9) Conclusion Remarks.

HYPOTHESIS

A microchannel heat sink device (MCHSD) with forward triangular ribs can efficiently and effectively control the overheating of a multi-junction photovoltaic cell subjected to high levels of solar concentration (1000 suns) and can keep the solar cell temperature in very low range.

OBJETIVES

- Evaluate if a micro-scale cooling device can control the overheating of a multi-junction solar cell, subjected to high concentration.
- Implement a computational model (CFD) of microchannels with triangular ribs that allow to describe in detail the heat transfer and hydraulic behavior of the flow.
- Evaluate the temperature and effective power of a multi-junction solar cell subjected to high concentration level, cooled by a microchannel heat sink device with triangular ribs on sidewalls.

1. HCPV WITH ´PASSIVE COOLING SYSTEM.

A HCPV can be defined as a set of component that allow to concentrate DNI onto a small area occupied by a highly efficient solar cell (Figure-1). To concentrate the solar radiation reflective and refractive technologies are used, being the Fresnel lens the best choice in terms of concentration technology, due to its advantages such as small volume, light-weight, and mass production with low cost, as well as, effective increase of the energy density [22]. A secondary lens is used to uniformly distribute the sunlight onto the solar cell. HCPV system concentrates the direct solar radiation between 300 to 1000 suns onto the solar cell. The concentrated DNI is absorbed by a HCPV receiver that is formed by different layers, where the principal layer corresponds to a multi-junction solar cell, which is a package of three solar cells connected in series (GaInP/GaInAs/Ge), where each cell has a different bandgaps, which allows to convert a greater part of the solar spectrum, so that each diode of solar cell going from the top to the bottom has smaller bandgap than the previous, and so it absorbs and convert the photons that have energies greater than the bandgap of that layer and less than the bandgap of the higher layer. In the HCPV receiver the top layer is the multi-junction solar cell, which is connected to a Direct Bonded Cooper (DBC) substrate using a lead-free SnAgCu solder, and then, DBC is bonded to a heat sink using a thermal interface material (TIM). The passive heat sink seeks to avoid the overheating of the solar cell and normally the passive cooling technique employed corresponds to a flat plate heat sink that is considered for the present analysis. The thickness of each layer that forms the HCPV receiver have been selected from [1] and are presented in Table-1.

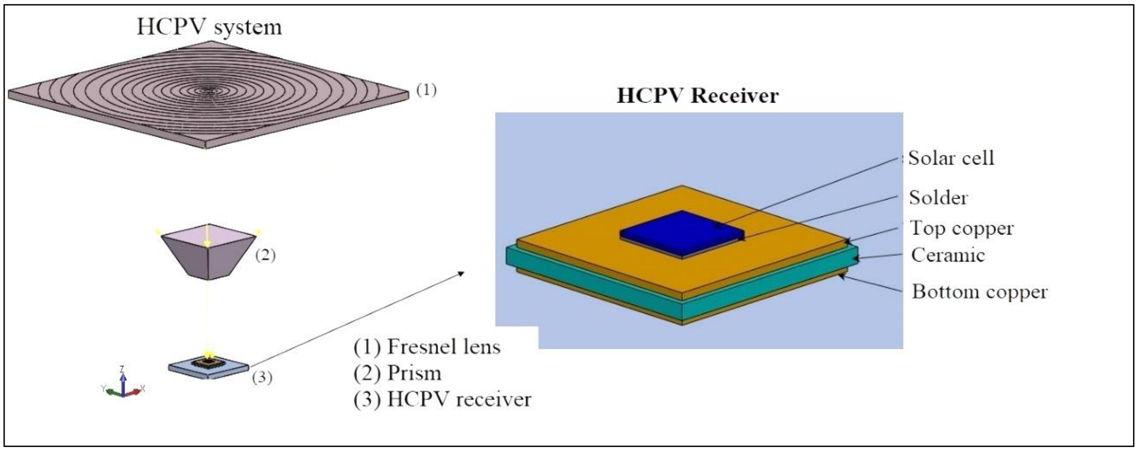

Figure-1: HCPV system with passive cooling system.

The multi-junction solar cell taken into account, in this work, has an area equivalent to 3x3 mm^2, which is the smallest cells commercially available nowadays [1]. A square flat plate was considered as passive cooling system, where the material corresponds to aluminum and three different sizes were evaluated (table-2). With respect to a thermal model of the multi-junction solar cell, it is possible to assume that the solar cell is a single block of Germanium (Ge) [1], due to the bottom cell is wider than the top and middle cells. We assume that all the heat generated by the solar cell is transferred by pure conduction through the different layers that conform the HCPV receiver to the heat sink. The heat sink refrigerates the HCPV receiver exchanging heat with the environment by radiative and convective. Finally, we despise the heat transferred by radiation and convection in the solar cell and DBC with the environment, because their small size compared with the heat sink.

$$k_i \nabla^2 T_i + q_{heat} = 0 \quad (1)$$

$$q_{heat} = CF * \eta_{optical} * DNI(1 - \eta_{solar\ cell}) \quad (2)$$

Table-1: Structure of HCPV receiver [1].

HCPV layer receiver			
Layer	**Material**	**e (mm)**	**W/m*K**
Solar cell	Ge	0.2	60
Solder	SnAgCu	0.125	78
Top copper	copper trace	0.3	400
Ceramic	AlNi	0.63	285
Bottom copper	copper trace	0.3	400
Heat sink	Al	4	229

The parameter k_i represents the thermal conductivity of the layer I and q_{heat} corresponds the heat generated per unit volume of the solar cell, due to the absorption of the solar radiation and a conversion efficiency which is initially considered equivalent to 40%. The CF, DNI and $\eta_{optical}$ are the concentrator factor, DNI, and optical efficiency of the Fresnel lens, respectively. The CF considered for the analyses is 1000x, the DNI is assumed equal to 1061 W/m^2, and the $\eta_{optical}$ is assumed equivalent to 89%. On the other hand, radiative and convective heat fluxes are applied to both the upward and downward surfaces of the heat sink. The convective heat coefficient is defined as follows based on [23], being k the thermal conductivity of the surface air, L_c is the characteristic length, defined as the ratio between the area and perimeter of the heat sink, and Ra_L is the dimensionless Rayleigh number, where $g$is the gravitational acceleration, β is the thermal expansion of the surrounding air, v is the kinematic viscosity and Pr is the Prandalt number.

$$hc = \frac{k}{L_c} 0.54 Ra_L^{0.25} \rightarrow \text{Upward facing surface if } Ra_L \leq 10^7 \tag{3}$$

$$hc = \frac{k}{L_c} 0.154 Ra_L^{0.33} \rightarrow \text{Upward facing surface if } Ra_L > 10^7 \tag{4}$$

$$hc = \frac{k}{L_c} 0.27 Ra_L^{0.25} \rightarrow \text{Downward facing Surface} \tag{5}$$

$$Ra_L = \frac{g\beta(T_{HS}-T_\infty)L_c^3}{v^2}\text{Pr};\ L_c = {}^{A_s}/_{P} \tag{6}$$

$$q_{conv} = h_c(T_{HS} - T_\infty) \tag{7}$$

$$q_{rad} = \varepsilon\sigma F_{ij}(T_{HS}^4 - T_{surr}^4) \tag{8}$$

The contribution of radiative heat flux of the flat plate with the surrounding is considered using the Stefan–Boltzmann equation, where ε is the emissivity of the flat plate that corresponds equivalent to 0.09 (polished aluminum), σ is the Stefan–Boltzmann constant ($5.67 * 10^8\ W/m^2 * K^4$), $F_{ij}$is the view factor between surface (upward and downward) flat plate and the surrounding, T_{surr} is the surrounding air temperature, and T_{HS} is the heat sink surface. For the present analysis, we considered a view factor equivalent to 1, which means that the surface j completely envelops the surface i, so that all the radiation that is emitted by the flat plate is intercepted by the environment, as well as the surrounding medium is considered to be a black body, so that $T_{surr} = T_{amb}$. Finally, the software COMSOL 5.1 Multiphysics was used to implement the thermal analysis of a HCPV with a flat plate as passive cooling system considering three sizes and different surrounding temperature (298 K to 328 K). The solution methodology, convergence criterion, numerical validation, and result are presented below.

TableN°2: Flat plate heat sink dimensions.

Heat sink	**size**	**Material**	**P (m)**	**As (m^2)**	**Lc (m)**
FPHS-A	50x50 mm	Al	0,2	0,0025	0,0125
FPHS-B	100x100 mm		0,4	0,01	0,025
FPHS-C	150x150 mm		0,6	0,0225	0,0375

2. MICROCHANNEL HEAT SINK DEVICE INCORPORATED IN A HCPV SYSTEM.

The present work proposes to incorporate a MCHSD consisted of 30 parallel microchannels with forward triangular ribs installed on the inner sidewalls of the channel to act as the refrigeration system of a multi-junction solar cells subjected to a high solar concentration level of 1000 suns. The total area of the MCHSD was equivalent to the total area of the multi-junction solar cell. The proposed MCHSD was incorporated on the bottom surface of the multi-junction solar cell as is shown in Figure-2, where the MCHSD is directly in contact with the solar cell assuming a negligible thermal contact resistance. The material of the microchannel cooling device was silicon and was incorporated in the back side of the Ge solar cell in the manufacturing process of the full HCPV receiver. The interfacial thermal resistance or Kapitza resistance(R_k) between Si-Ge tends to a constant value of $8.143 * 10^{-9}$ $[m^2 * K/W]$. When the length of Si or Ge in the interface is higher than 50 nm [27] and the length scales employed in our model for the microchannel and solar cell are much greater than 50 nm, we assumed a negligible thermal contact resistance for all analysis because of the small value of the interfacial thermal resistance compared with that of the thermal resistance by conduction. Consistently, with the aforementioned , Radwan and Ahmed [6] simulated and analyzed smooth microchannels as cooling system applied to low concentration PV cells with negligible thermal contact resistance. Their results were validated by means of available experimental and numerical data. Although more detailed investigation and studies of the effect of the interfacial resistance on the thermal performance are important, they are beyond the scope of this article. The multi-junction solar cell taken into account measured 3x3 mm^2. Each microchannel of the MCHSD has a total length (L) of 3 mm. The proposed integration did not affect the normal operation of the HCPV receiver, and the electrical connections allowed normal operation. The present study was not concerned with the manufacturing techniques or processes to proposed integration. Finally, as the proposed MCHSD was to be in direct contact with the solar cell, the heat generated by the solar cell is completely transferred to the MCHSD.

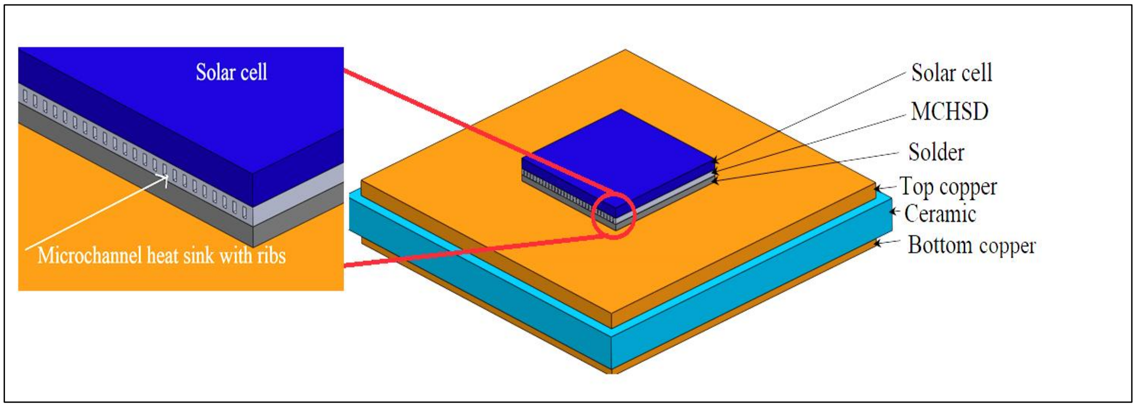

Figure-2: Integration proposed between multi-junction solar cell and a MCHSD system.

3. MICROCHANNEL DOMAIN AND NUMERICAL METHOLOGY

To determine the performance of the proposed MCHSD with microchannels that have triangular ribs mounted on the inner sidewalls. Numerical simulations of a microchannel with and without ribs were carried out, considering a three-dimensional solid-fluid domain subjected to a constant heat flux on the top surface of the microchannel (Figure-3), which is equal to the heat generated by the solar cell considering a conversion efficiency equivalent to 40%. The total length of the computational domain analyzed (L) corresponds to 3 mm (the length of the domain is equivalent to the total length of a multi-junction solar cell), the width (W) and the height (H) are of 83μm and 117μm, respectively. The solid material considered for the microchannel corresponds to Silicon and the coolant employed in the simulation was water in single-phase and laminar regimen. It is important to mention that it is assumed that each microchannel that forms the MCHSD does not affect thermally adjacent microchannels.

To analyze the effect of the triangular ribs in terms of hydraulic and thermal performance, three microchannel domains have been simulated (Figure-4), where two of these computational domains correspond to a microchannel with triangular ribs, considering aligned and offset distribution of the ribs along the inner sidewalls of the microchannel. The other domain corresponds to a smooth microchannel (SMC). The fluid domain in the microchannel has been built considering a total length (L), height (Hc), and width (Wc) equivalent to 3 mm, 67μm, and 33μm, respectively. With respect to the ribs, forward triangle shaped with a height (hc) and base (ac) equivalent to 8.3 μm and 16.7 μm, respectively, have been mounted on the inner sidewalls of the microchannel.

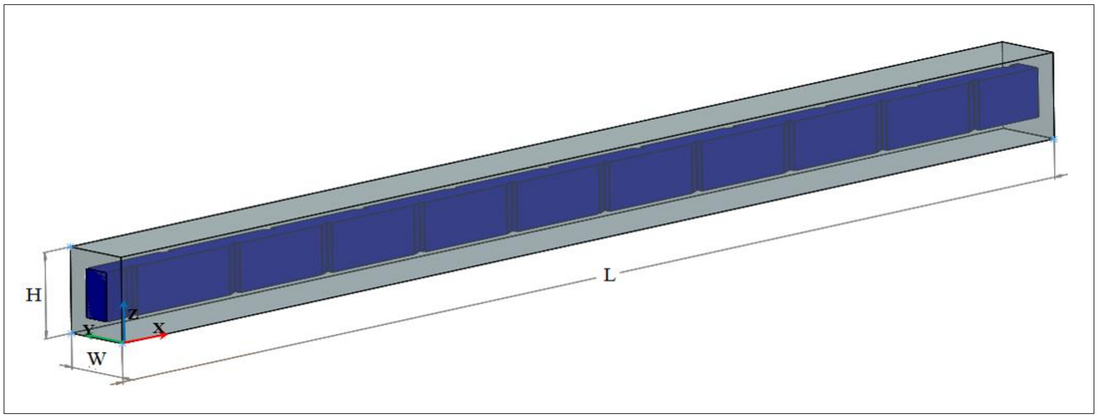

Figure-3: Computational domain with offset triangular ribs mounted on the inner.

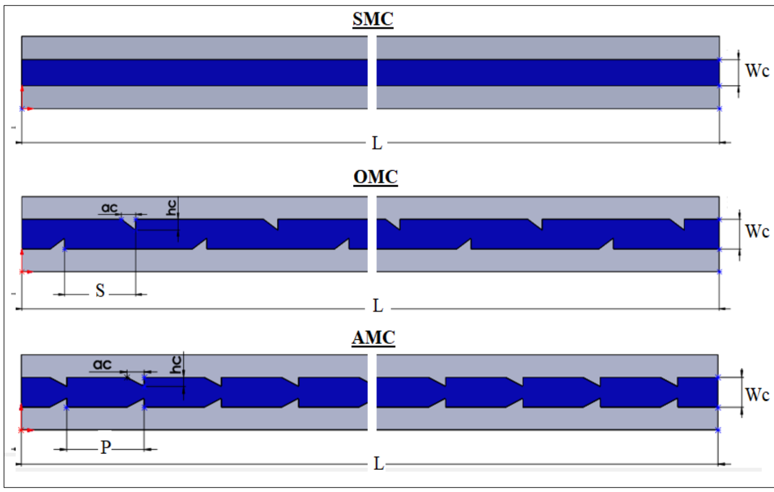

Geometric specifications		
L	3	mm
H	0.117	mm
W	0.083	mm
Hc	0.067	mm
Wc	0.033	mm
hc	0.0083	mm
ac	0.0167	mm
P	0.060	mm
S	0.0667	mm

Figure-4. Geometric specifications: Smooth MicroChannel (SMC), Offset MicroChannel (OMC), and Aligned MicroChannel (AMC).

The software COMSOL 5.1 Multiphysics was used to solve the governing equation in a conjugate heat transfer situation considering: (1) Incompressible flow; (2) Single-phase flow; (3) Laminar flow; (4) Steady analysis; (5) Isotropic thermal-physical properties (solid &liquid); (6) Flow properties dependency of temperature; (7) Radiation heat transfer is neglected; (8) the Knudsen number ($Kn = \frac{\lambda}{D_h}$) is lower than 0.001[24], therefore, the continuum hypothesis is respected for all fluid and solid domain. Considering the assumptions described before, the governing equations of mass, momentum and energy can be written as follows:

Continuity equation:

$$\frac{\partial(\rho_f u_i)}{\partial x_i} = 0 \tag{9}$$

Navier-Stoke equation:

$$\frac{\partial}{\partial x_i}\left(\rho_f u_i u_j\right) = -\frac{\partial p}{\partial x_i} + \frac{\partial}{\partial x_i}\left[\mu_f\left(\frac{\partial u_j}{\partial x_i} + \frac{\partial u_i}{\partial x_j}\right)\right] \tag{10}$$

Energy equation for the coolant:

$$\frac{\partial}{\partial x_i}\left(\rho_f u_i Cp_f T\right) = \frac{\partial}{\partial x_i}\left(k_f \frac{\partial T}{\partial x_i}\right) + \mu_f\left[\left(\frac{\partial u_i}{\partial x_i}\right)^2 + \left(\frac{\partial u_j}{\partial x_i} + \frac{\partial u_i}{\partial x_j}\right)^2\right] \tag{11}$$

Energy equation for the solid:

$$k_s\left(\frac{\partial^2 T}{\partial x_i \partial x_i}\right) = 0 \tag{12}$$

Where ρ_f is the flow density, μ_f is de dynamic viscosity, Cp_f is the flow specific heat capacity, k_f is the flow thermal conductivity, and k_s is the solid thermal conductivity. On the other hand, $i = 1,2,3$; x_1, x_2, and x_3 are x, y and z coordinates, respectively, as well as u_1, u_2 and u_3 are u, v and w velocities.

A three-dimensional solid-fluid domain is studied, where water was used as coolant considering incompressible flow, single-phase, laminar condition, isotropic and dependency of the fluid properties with respect to the temperature. On the other hand, silicon was considered for the solid, where its thermal conductivity is constant and equal to 148 W/m*K and. Based on F.P. Incropera [22], the thermal-physical properties of the fluid are calculated using the following correlations.

$$\rho_f = \frac{999{,}84+18{,}225\,T-7{,}92*10^{-3}T^2-5{,}545*10^{-5}T^3+1{,}498*10^{-7}T^4-3{,}933*10^{-10}T^5}{1+1{,}816*10^{-2}T} \quad (13)$$

$$k_f = -0{,}58166 + 6{,}3556 * 10^{-3}T - 7{,}964 * 10^{-6}T^2 \quad (14)$$

$$\mu_f = 2{,}414 * 10^{-5} * 10^{\frac{247{,}8}{T-140}} \quad (15)$$

$$Cp_f = 8958{,}9 - 40{,}535\,T + 0{,}11243T^2 - 1{,}014 * 10^{-4}T^3 \quad (16)$$

Where T is the fluid temperature. For equation-13 T is in Celsius degrees and equations 14 to 16 the temperature is in Kelvin scale. The property boundary conditions (Figure-5) employed for solving the governing equations are:

a) Inlet velocity boundary condition (u_{in}): The average velocity of the flow is considered at the inlet of the microchannel (x=0 mm). The inlet velocity is determined through Reynolds number, where the Reynolds's values considered are 100,200,300, and 400.

b) Inlet temperature boundary condition (T_{in}): $x = 0 \rightarrow\ T_{in} = 293\ [K]$

c) Outlet pressure boundary condition (P_{out}): A constant pressure is applied at the microchannel outlet (x=L).Where the value of P_{out} corresponds to a null gauge pressure.

d) Outflow boundary condition: on the outlet of the microchannel ($x = L$).

e) For the inner wall/fluid interface surface: two boundaries conditions are applied. First, the velocity for x, y and z direction are zero due to the non-slip condition.

Second, the heat transfer by conduction in the solid is equal to the heat transfer by conduction on the liquid

$$u = v = w = 0$$

$$-k_s \frac{\partial T_s}{\partial n} = -k_f \frac{\partial T_f}{\partial n}; n\ is\ the\ coordinate\ normal\ to\ the\ wall$$

f) Insulation boundary: at the two sides of the computational domain, a null normal gradient of temperature for the symmetry planes.

$$y = 0 \rightarrow \frac{\partial T_s}{\partial y} = 0;\ y = W \rightarrow \frac{\partial T_s}{\partial y} = 0$$

g) Constant heat flux boundary condition (q_w): on the upper wall of the computational domain a constant heat flux is applied. The magnitude of q_w depends of the initial conversion efficiency ($\eta_{solar\ cell} = 40\%$) of the triple junction solar cell and the solar radiation concentrated onto the HCPV receiver.

$$z = H \rightarrow\ q_{heat} = -k_s \frac{\partial T}{\partial z}$$

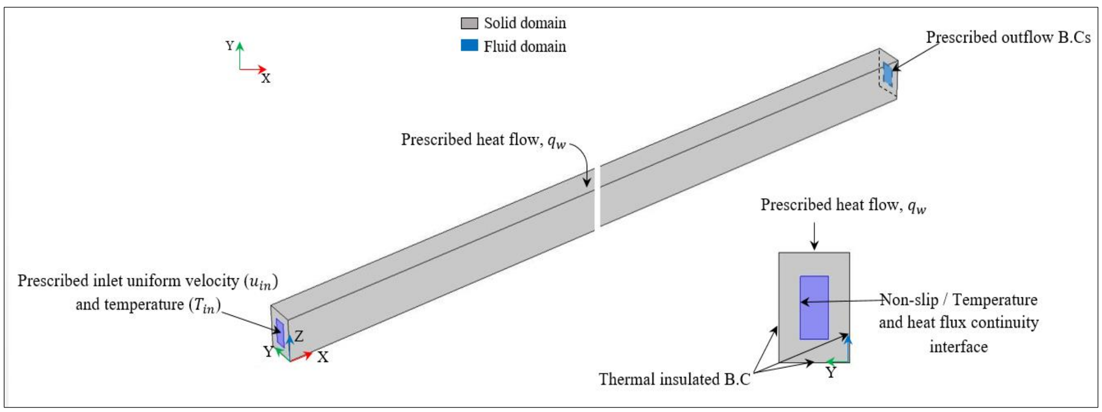

Figure-5: Fluid and Heat transfer boundary conditions on the microchannel domain.

5. SOLUTION METHOLOGY AND CONVERGENCE TEST

The numerical simulations are performed using COMSOL-Multiphysics 5.1 software which solves the governing equations using the finite element method. The numerical stabilization employed for solving the governing equations were streamline and crosswind [29]. With respect to the discretization, tetrahedral elements were used, specifically, linear elements (P1) for the temperature and pressure field and quadratic elements (P2) for the velocity field. However, in the case of the HCPV receiver with FPHS, the discretization of the domain of the temperature profile was performed using quadratic elements. For conjugate heat transfer-laminar problems, a segregate solver was used. The damped Newton method was used and a nonlinear solver and a pseudo-time stepping method were invoked by improving the convergence in the solution of the Navier-Stokes equation, using the default parameters suggested by COMSOL-Multiphysics 5.1 for the Courant number (CFL). Finally, the generalized minimal residual algorithm was employed to solve the non-symmetry equation system.

To verify the numerical solution, a grid independence test is conducted using several mesh sizes. The convergence rate was evaluated based on the relative percentage error (E_{rr}) in different points of the domain. For example, when Re=400, the minimum relative error of the velocity in the offset microchannel (OMC) and aligned microchannel (AMC) configurations was 5.3% using 4 million DoFs (Figure-6a) and 6.4 % (Figure-6b) using 4.4 million DoFs, respectively. With respect to the HCPV with FPHS (Figure-7), the relative error of the average temperature of the solar cell was lower than 1% for all the meshes analyzed.

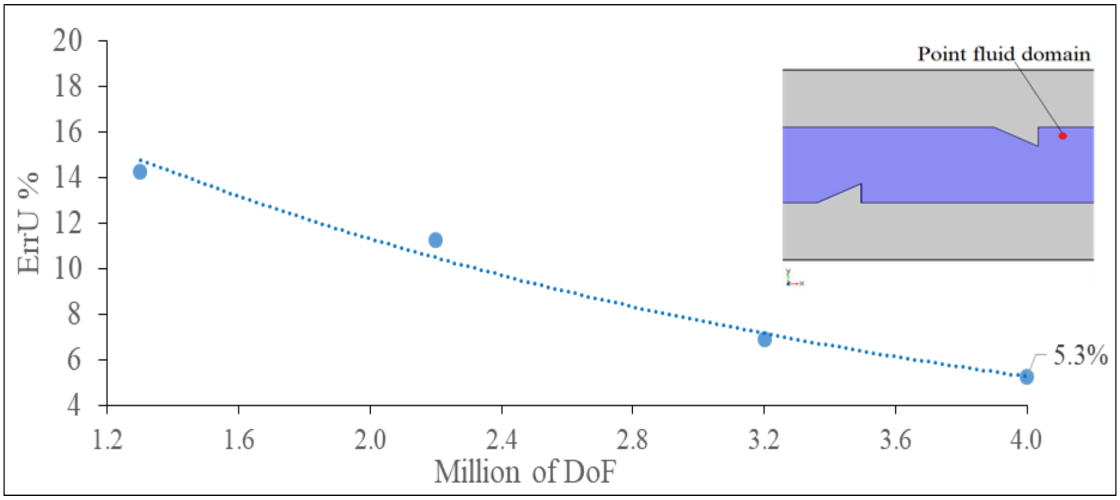

Figure-6a: Convergence test Re= 400. Relative error of velocity in Offset MCH.

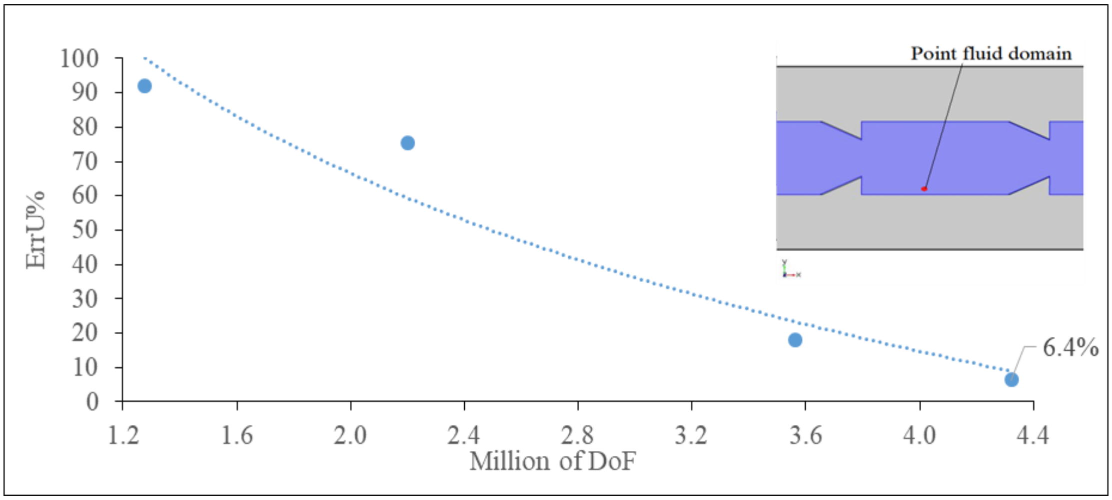

Figure-6b. Convergence test Re= 400. Relative error of velocity in ACM. Point fluid domain (x=1500 μm;y=2.75 μm;z=33 μm)

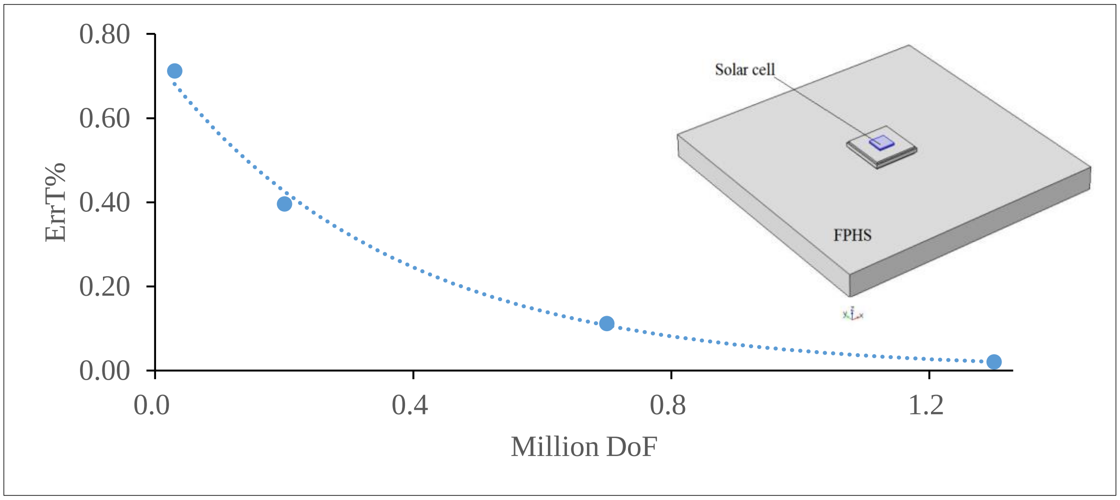

Fgure-7. Convergence test. Relative error of average solar cell temperature for FPHS of 100x100mm^2.

The numerical simulations are performed using the COMSOL-Multiphysics 5.1 software, which solves the governing equations using the finite element method (FEM). The numerical stabilization employed by solving the governing equation corresponds, streamline and crosswind [25]. With respect to the discretization in the microchannel domain, tetrahedral elements were used. Linear elements (P1) for the temperature and pressure field. Moreover, quadratic elements (P2) for the velocity field On the other hand, in the case of the HCPV receiver with flat plate heat sink the discretization of the domain of the temperature profile was carried out using quadratic elements. For conjugate heat transfer-laminar problems a segregate solver is used. The damped Newton method is used as the nonlinear solver and the pseudo-time stepping method is invoked by improving the convergence in the solution of the Navier-Stoke equation, using the default parameters suggested by COMSOL-5.1 to the Courant number (CFL).Finally, the Generalized Minimal Residual algorithm (GMRES) was employed to solve the non-symmetry equation system.

To verify the numerical solution, a grid independence test is conducted using several different mesh sizes, where the procedure for achieving the convergence consists in increasing the degrees of freedom (DoFs). The convergence rate is evaluated based on the relative percentage error (E_{rr}) in different points of the domain. For example, in the microchannel domain with offset ribs (Figure-6a), when Re=400 the relative error of the velocity decreases to a value lower than 5.5% for the point presented below (x=1500 μm;y=29.1 μm;z=33 μm), using meshes with 0.07, 0.57, 1.3, 2.2, 3.2, and 4 millions Degree of Freedoms (DoFs). In the same way, for microchannel with aligned ribs (Figure-6b), the minimum relative error reached is 6.4% for the point of the domain showed below (x=1500μm;y=2.75 μm;z=33 μm), which is achieved with 0.07, 0.57, 1.3, 2.2, 3.6, and 4.3 millions Degree of freedom. With respect to the HCPV with flat plate heat sink (Figure-7), the relative error of the average temperature of the solar cell convergence fast, being lower than 1% for all the meshes sizes analyzed with 0.008, 0.03, 0.2, 0.7, 1.1 million DoFs,

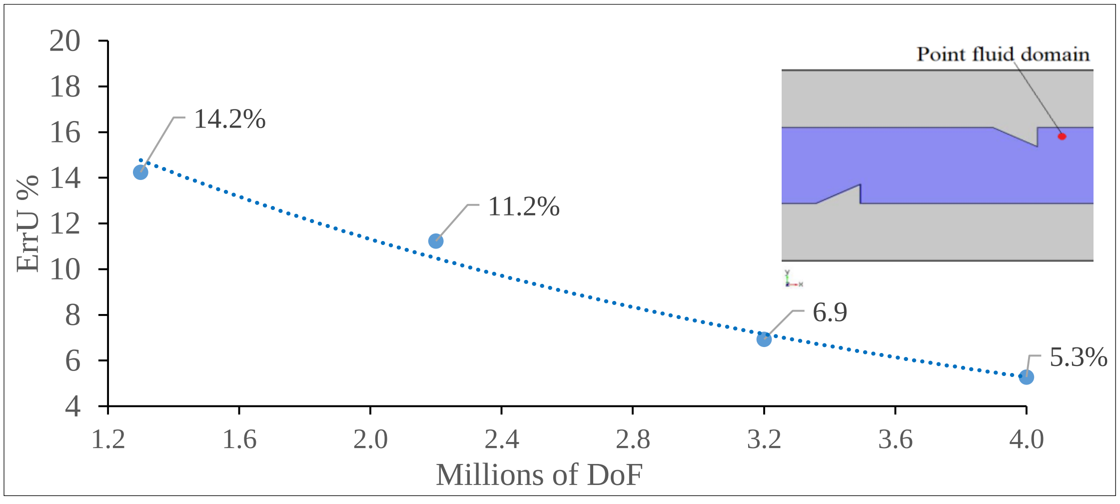

Figure-6a: Convergence test Re= 400. Relative error of velocity in Offset MCH.

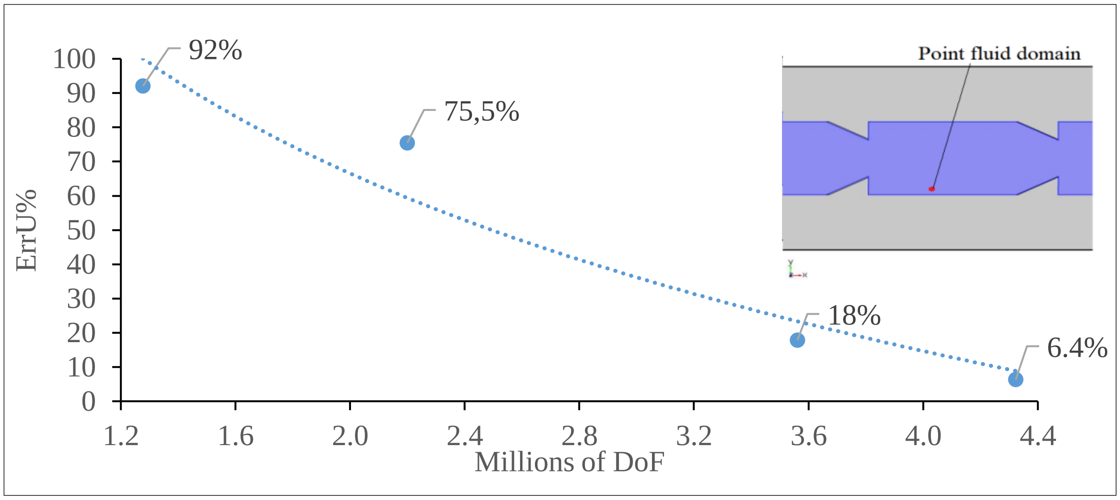

Figure-6b: Convergence test Re= 400. Relative error of velocity in Aligned MCH.

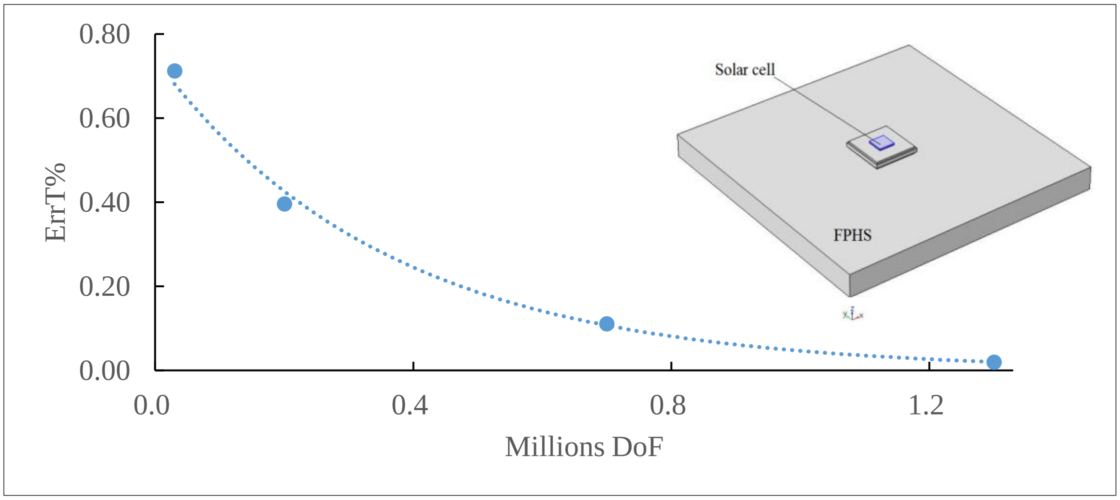

Figure-7: Convergence test. Relative error of average solar cell temperature for FPHS of $100x100mm^2$.

6. RELEVANT PARAMETERS.

In order to evaluated the thermal and hydraulic performance of the microchannels evaluated and the thermal performance of the flat plate considered as passive cooling system, definitions are presented for calculating fluid flow and heat transfer characteristics.

6.1-FPHS data acquisition.

- Solar cell power.

$$W_{SC} = CF * \eta_{optical} * DNI(\eta_{solar\ cell})A_{cell} \quad (17)$$

- Global thermal resistance passive heat sink (FPHS).

$$R_{th,FPHS} = \frac{\bar{T}_{SC} - \bar{T}_{surr}}{q_{heat}} \quad (18)$$

- Total heat transferred by flat plate heat sink with the surrounding.

$$Q_{FPHS} = 2\sigma\varepsilon A_s(\bar{T}_{FPHS}^4 - T_\infty^4) + A_s(\bar{T}_{FPHS} - T_\infty)\left(h_{c,upward} + h_{c,downward}\right) \quad (19)$$

6.2.-Microchannel data acquisition.

- Reynolds number:

$$R_e = \frac{\rho_f \bar{u}\ D_h}{\mu_f} \quad ((20)$$

Where $\rho_f$is the volume-average fluid density, $\bar{u}$ is the average flow velocity, D_h is the hydraulic diameter calculated based on the channel section of the smooth microchannel, μ_f is the dynamic viscosity.

$$D_h = \frac{2H_cW_c}{H_c + W_c} \quad (21)$$

- Apparent average and local friction factor in the microchannel:

$$\bar{f}_{app} = \frac{\Delta P D_h}{2\rho_f L \bar{u}^2} \tag{22}$$

$$f_x = \frac{(p_{in} - p_x) D_h}{2\rho_f x \bar{u}^2} \tag{23}$$

Where L is the total length of the microchannel (3 mm), ΔP is the pressure drop along the microchannel. p_{in} is the mass weighted average pressure in the channel inlet, x is the length of the microchannel where is analyzed the friction coefficient and p_x is the pressure in the channel outlet at the x position.

- For developing laminar flow, the friction factor according to Steinke & Kandlikar Ref[26] takes into account the pressure drop due to friction and the developing region effects, given by:

$$f_{app} = f + \frac{K(\infty) D_h}{L_t} \tag{24}$$

Where f is the friction factor for a fully developed flow. Shah and London Ref[27] provide the following equation for a rectangular channel with short side *a* and long side *b*, and a channel aspect ratio defined as α=*a*/*b*, based on the Poiseuille number. $K(\infty)$, known as Hagenbach's constant factor. Steinke and Kandlikar Ref[26] obtained the following curve-fit equation for the Hagenbach's factor for rectangular channels:

$$P_o = f * Re = 24(1 - 1{,}3553\alpha_c + 1{,}9467\alpha_c^2 - 1{,}7012\alpha_c^3 + 0{,}9564\alpha_c^4 - 0{,}2537\alpha_c^5) \tag{25}$$

$$K(\infty) = 0{,}6796 + 1{,}2197\alpha_c + 3{,}3089\alpha_c^2 - 9{,}5921\alpha_c^3 + 8{,}9089\alpha_c^4 - 2{,}9959\alpha_c^5 \tag{26}$$

- The local heat transfer coefficient and Nusselt number:

$$h_x = \frac{q_w(W*x)}{A_{cond}(T_{w,x}-T_{f,x})} \tag{27}$$

$$Nu_x = \frac{h_x D_h}{k_f} \tag{28}$$

Where W is the width of the microchannel and x is the length where is analyzed the heat transfer coefficient. $A_{cond,x}$ is the inner wall/ fluid contact surface area, $k_f$is the fluid thermal conductivity, $T_{w,x}$ and $T_{f,x}$ are the local area-weighted temperature of the silicon upper face and the local mass-average temperature of water in microchannels, defined as:

$$T_{f,x} = \frac{\int T_{f,x}\rho_f|\vec{u}d\vec{A}|}{\int \rho_f|\vec{u}d\vec{A}|} \tag{29}$$

$$T_{w,x} = \frac{\int T_{w,x,y}dy}{\int dy} \tag{30}$$

- The average heat transfer coefficient and Nusselt number:

$$\bar{h} = \frac{1}{L}\int h_x\, dx \tag{31}$$

$$\bar{N}_u = \frac{1}{L}\int Nu_x\, dx \tag{32}$$

The outlet flow temperature in the microchannel, is obtained by an energy balance, given by:

$$T_{out} = T_{in} + \frac{q_w W L}{\rho\, A_{in}\, \overline{u}\, cp} \tag{33}$$

Where A_{in}, ρ_f, and cp_f are the inlet area of the microchannel, the average density and specific heat of water, respectively.

• Pumping power and global thermal resistance of the MCHSD.

$$W_{p,MCHSD} = \Delta P * \dot{\forall} * \#_{MC} \tag{34}$$

$$R_{th,MCHSD} = \frac{(\bar{T}_w - T_{in})}{q_{heat}} + \frac{e_{SC}}{k_{SC}} \tag{35}$$

Where, $\dot{\forall}$ is the volumetric flow rate, ΔP is the total pressure drop and $\#_{MC}$ is the number of parallel microchannel. With respect to the global thermal resistance, $\bar{T}_w$ is average temperature of the silicon upper face area, and T_{in} is the temperature of water in the inlet microchannels.

• Effective solar cell (SC) power and temperature (W_{SC} in Eq-17).

$$P_e = W_{SC} - W_{p,MCHSD} \tag{36}$$

$$\bar{T}_{sc} = \bar{T}_{w;MCHSD} + \frac{e_{SC}}{k_{SC}} * q_{heat} \tag{37}$$

7. NUMERICAL VALIDATION

In order to verify and ensure the numerical simulations and its accuracy, we analyzed characteristic parameters getting form the simulations and we compared it with theoretical solution.

7.1.-FPHS numerical validation

The average temperature of the flat plate heat sink (T_{FPHS}) determined through the numerical simulations is validate using Eq-19, which is a non-lineal equation that represent the physic that involves the heat transfer in FPHS with the surrounding. Figure-8.9 &10 show the behavior of the T_{FPHS} with respect to different surrounding temperatures (T_{amb}). For the three flat plate areas considered. It is possible to see the good agreement between the numerical solution and the temperature determined by Eq-24, which is lower than 1%.

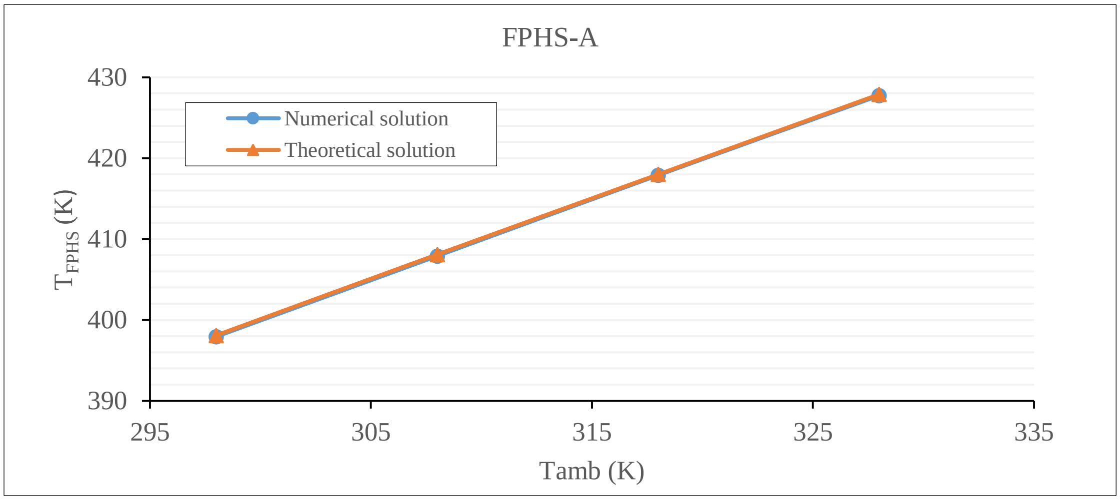

Figure-8: Numerical and theoretical data average temperature of FPHS-A.

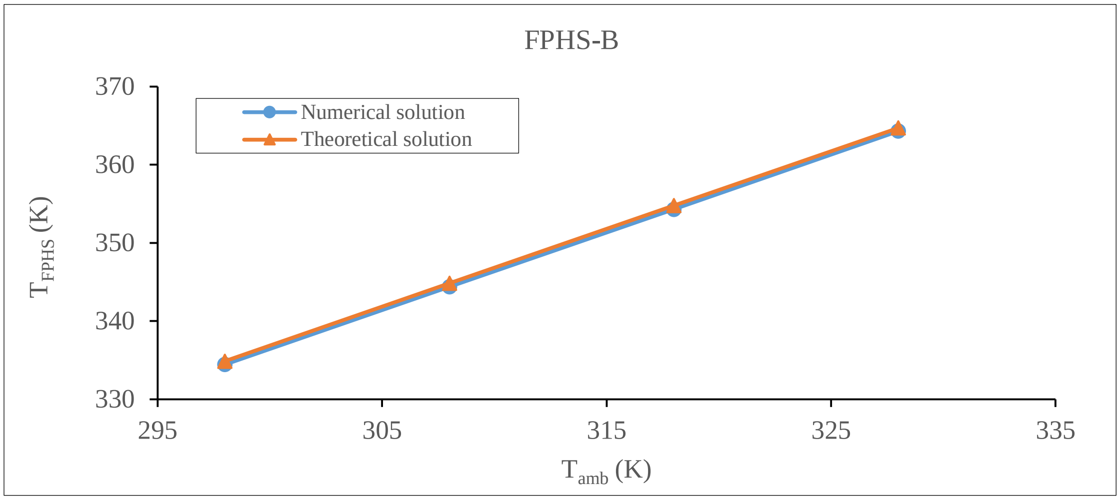

Figure-9: Numerical and theoretical data average temperature of FPHS-B.

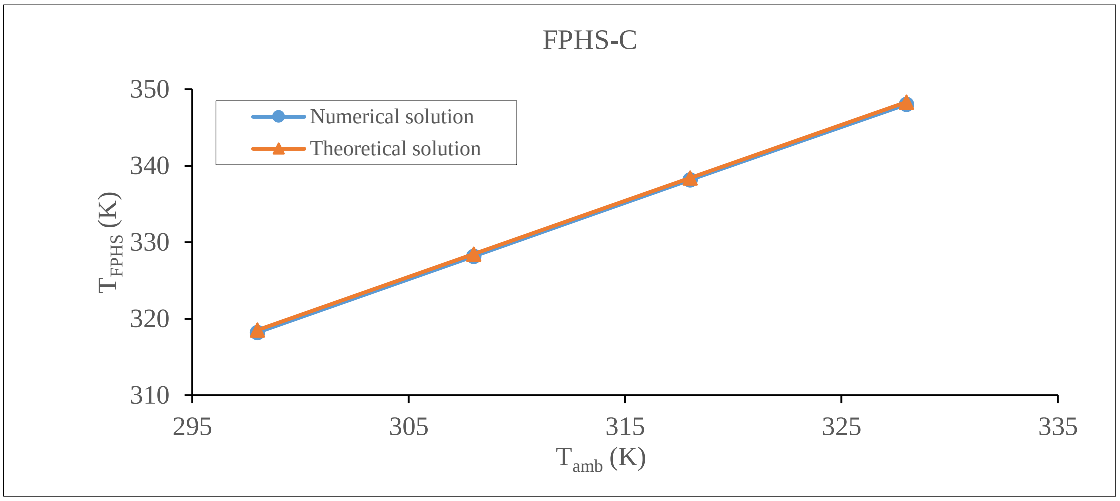

Figure-10: Numerical and theoretical data average temperature of FPHS-C.

7.2.-Microchannel numerical validation.

The friction factor and outlet flow temperature of the smooth microchannel are compared with the theoretical solutions. The theoretical solution of the apparent friction factor and outlet flow temperature are obtained from Equations (24) and (33), respectively. Figures-11 and Figure-12 show a comparison between numerical and theoretical results with varying Reynolds number (100 to 400). It can be clearly seen that the numerical results are in good agreement with the theoretical data at all given Reynolds, where the maximum relative error between numerical and theoretical results of apparent friction factor and outlet flow temperature are less than 13% and 7%, respectively. Therefore, the present numerical method can be able to accurately predict the fluid flow and heat transfer performance for the microchannel heat sink studied in the present work.

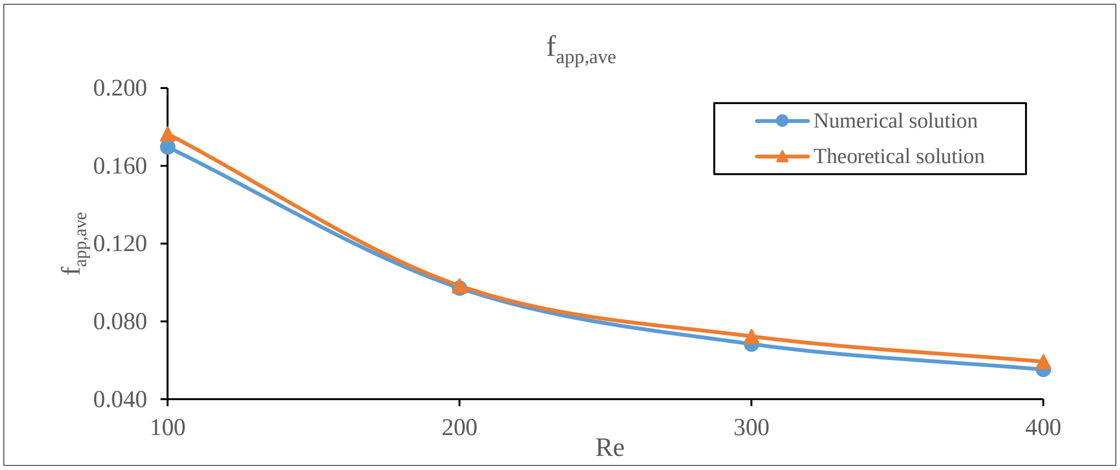

Figure.11: Numerical and theoretical data of average friction coefficient versus Re.

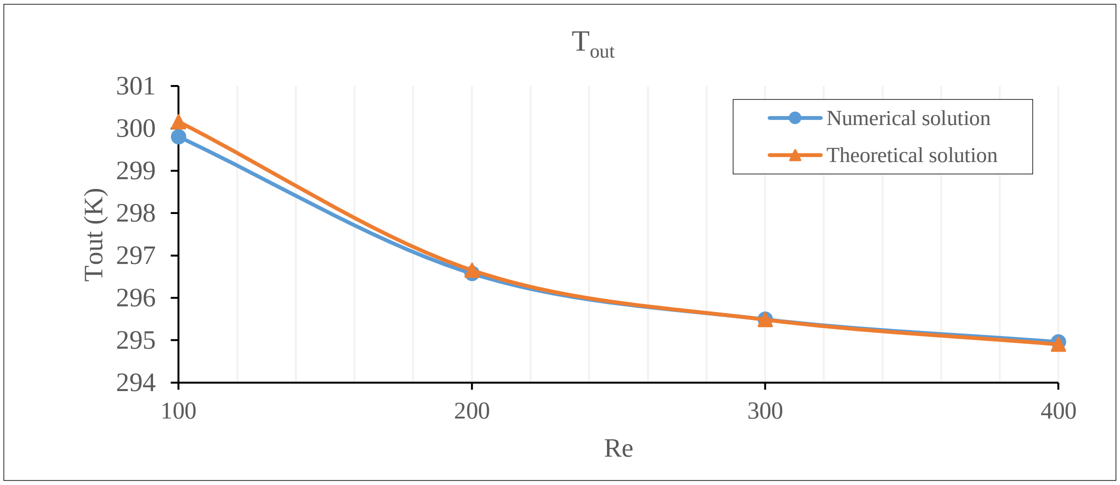

Figure.12. Numerical and theoretical data of the outlet fluid temperature versus Re.

8. RESULTS AND DISCUSSIONS

The analyzed microchannels with ribs have been proposed as cooling option for a high concentration photovoltaic system against a flat plate heat sink. To continue we analyzed the performance of microchannel with ribs and the HCPV with a flat plate heat sink, as well as we compare both system based on the solar cell.

8.1.-HCPV with FPHS.

Three sizes of flat plate heat sink (FPHS) were analyzed numerically considering different surrounding temperatures (298 K to 328 K). Figure-13 presents the average cell temperature for the different surrounding temperatures considered in the simulations. Figures-14 shows the temperature distribution on the HCPV system associated with a surrounding temperature equal to 298 K. Based on the data, an important dependence of the solar cell temperature is shown with respect to the dimension of the FPHS and the surrounding temperature. As the FPHS increases its area and the surrounding temperature decreases, the solar cell temperature decreases as well. Therefore, the smallest flat plate heat sink (FPHS-A 50x50 mm2) generates the highest solar cell temperature for all range of surrounding temperature considered, being the maximum T_{SC} = 432 K when T_{surr}= 328 K and minimum T_{SC} = 403 K when T_{surr} = 298 K , which means that FPHS-A generates hazardous condition of operation in the solar cell that can damage its components. The FPHS-C has the greatest heat transfer area with $T_{SC} < 354$ K C when T_{surr} = 328 K, as well as when T_{surr}= 298 K the average solar cell temperature corresponds to 324 K, which compared with FPHS-A the FPHS-C reduce the solar cell temperature in 79 K. The

T_{SC} reached with FPHS-B is 16 K higher than T_{SC} achieved with FPHS-B, and T_{SC} lower 63 K compared with the FPHS-A. Based on Figure-13 it is possible to conclude that the solar cell temperature increases linearly with the increment of the surrounding temperature, independently of heat sink size. The passive cooling system evaluated has problems to keep the solar cell temperature in low range and it has a high dependency of the surrounding temperature. To keep the solar cell temperature in low ranges than the reported, for any surrounding temperature, the size of the flat plate should greater than FPHS-C, adding more extra weight to the HCPV system.

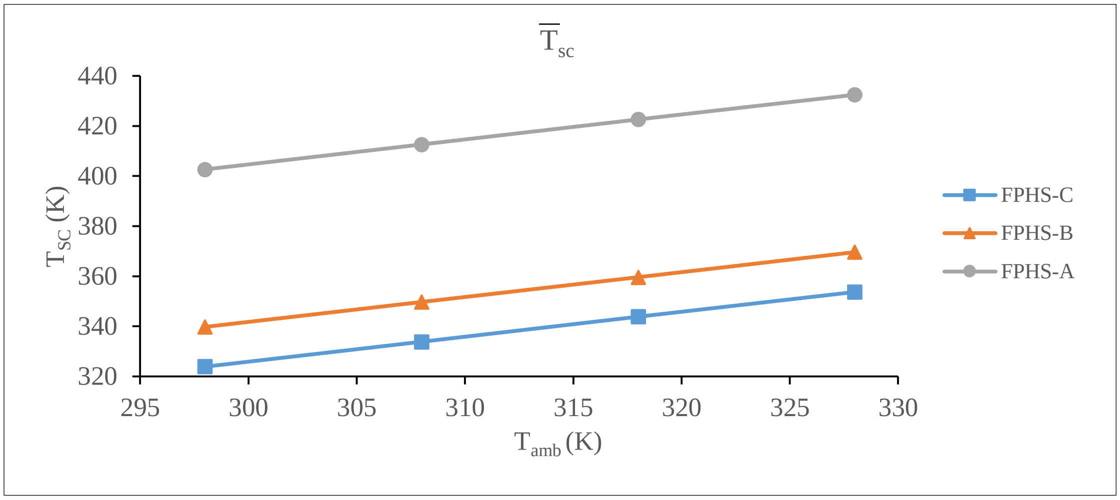

Figure-13: Average solar cell temperature considering passive cooling system at T_{surr}: 298K

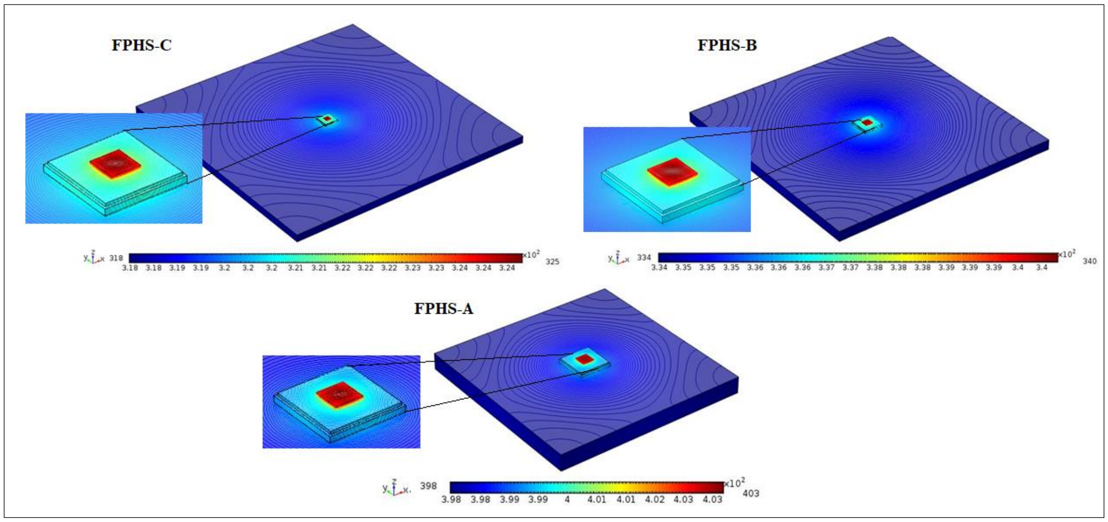

Figure-14: Temperature distribution in a HCPV at T_{surr}= 298K. FPHS-C (150x150 mm^2); FPHS-B (100x100 mm^2); FPHS-A (50x50 mm^2)

8.2.-Microchannel domain.

The numerical simulations carried out allow the evaluation of the proposed microchannels in terms of their thermal and hydraulic characteristics.

8.2.1-Flow structure.

Arrow and surface diagrams were used to analyze the flow structure in the microchannels, where the charts are given in the x-y plane (z = 33,5μm), considering Re =100 & 400. Based on the flow structure showed in Figure-15, it is noted that the use of triangular forward ribs produce important changes in the behavior of the flow with respect to the SMC, where the velocity profile seeks to be parabolic as expected to happen in a laminar flow. On the other hand, as the mainstream flow passes over the ribs the flow suffers a contraction and disturbance of its structure, being the clearest effects the acceleration of the flow current and the vortexes behind ribs.

The flow downstream from the ribs suffers the separation of its hydraulic boundary layer and flow recirculation occurs, which allow a mixture between the hot water near the wall and the cold water in the microchannel center in the y-direction. The flow behind the ribs require a specific length to redevelopment hydraulic boundary layer, where the reattachment length of the flow is function of the Reynold number, increasing in the x-direction when Re is higher, which means the length of the vortexes generated by the ribs are proportional to the flow velocity. For both microchannels with ribs, when Re= 100 the flow behind the ribs has enough distance for achieving the reattachment before next rib. On other hand, for Re=400 the flow in the aligned and offset configurations seem not to have enough distance between ribs to reach the reattachment. Based on Figure-16, in both configurations the ribs generate a reduction of the flow passage, which produces the acceleration of the flow, being higher in the AMC configuration because two ribs converge in the same point of the channel. After the flow has passed over the ribs, the flow is expanded, which produces a deceleration.

In the OMC configuration, the flow presents an oscillating movement, where the amplitude of this movement decreases when Reynolds increases, and then, higher velocities are achieved in the center of the channel, as well as the maximum velocity moves to the other sidewall without ribs when the flow is passing over a rib. With respect to the AMC configuration, the flow converges and diverges along the channel, presenting a flow structure much complex and with highest velocities in the channel center for all the Re range evaluated. Vortexes are created in both configuration, being higher and more influential as Reynolds increases. In AMC configuration parallel vortexes are created in the inner sidewall behind the ribs, therefore, the flow passage tends to suffer a constant contraction as Re increases, maintaining a higher velocity in the center of the channel, due to the length of the vortexes. For the microchannels with ribs, the minimum velocities always appears behind the ribs. By contrast, the SMC configuration presents its maximum flow velocity always in the microchannel center and the minimum velocity occurs near to the walls, due to the no-slip condition. The perturbation effect generated by the ribs in the flow structure has a limited effect in the core of the flow, because vortexes have a more local effect near to the side walls of the microchannel. In addition, small laminar stagnation could occur in the upstream of the ribs at very low Re, which can affect the heat transfer according to Ref[28] & Ref[29], however, by incrementing Re this condition must disappear. Finally, the microchannels with ribs present a chaotic behavior of the flow, which increases the heat transfer performance, on other hand, the flow structure has a periodical behavior along the microchannel with ribs, which allow to consider that the flow has the same structure along the channel.

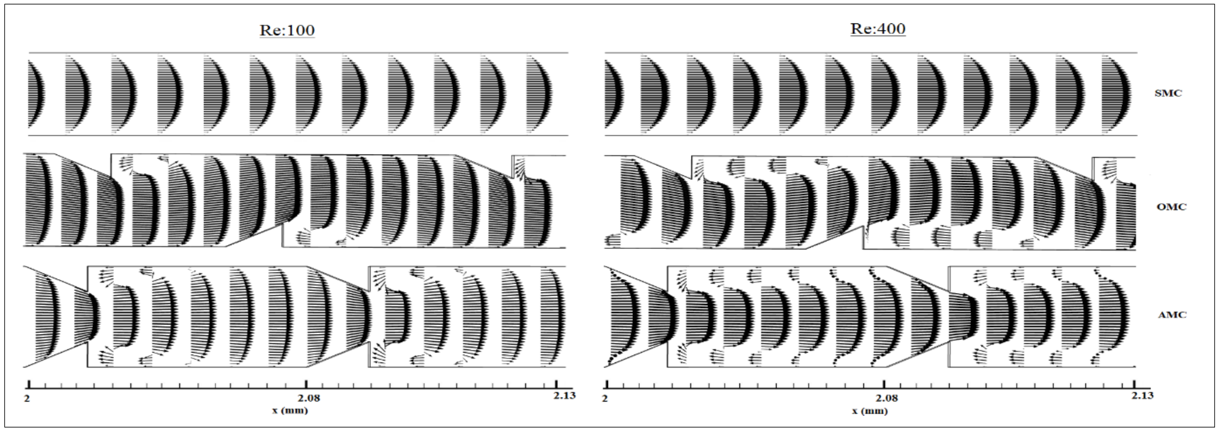

Figure-15: Flow structure in microchannel domains at Re= 100 & 400 (plane x-y; z=H/2).

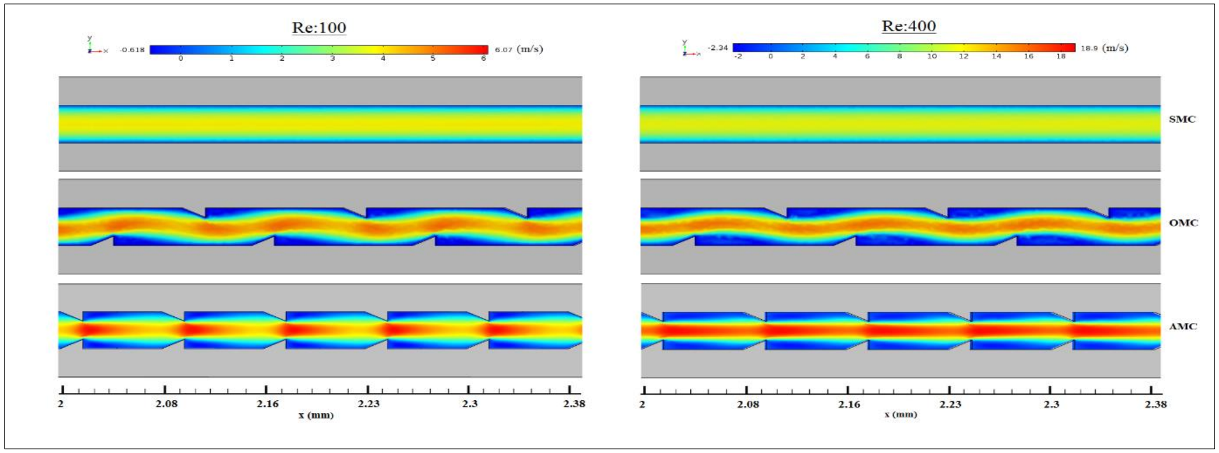

Figure-16: Velocity distribution in the microchannel domains at Re=100 & 400 (plane x-y; z=H/2)

8.2.2.-Pressure drop and friction factor.

Figure-17 shows the flow pressure in the x-direction along the microchannel for Re= 400, where it is possible to see that in the smooth microchannel heat sink (SMC) the pressure continuously decreases, because frictional losses along the microchannel occur; on the other hand, in the microchannels with triangular ribs the pressure drop is function of the frictional losses and the effect generated by the ribs. For both microchannels with ribs, the flow fluctuation due to the continuous sudden contraction and expansion have an important effect on the pressure drop, because in AMC and OMC pressure drop is mainly caused by the changed flow passage and the sudden contraction of the flow passage. As coolant flows across the ribs, the pressure rapidly decreases with the contraction of flow passage and slowly increases with the expansion of the cross section, however it is important to note that the contraction of flow passage results in a very high pressure drop, being the AMC configuration the microchannel with highest drop pressure than the two other configurations. In the recirculation zones, behind ribs, the pressure is lower due to the flow structure created, where velocity change its direction and its magnitude is minimum. The highest pressure drop occurs in the microchannel with aligned ribs, where the pressure drop is 8 times higher than in SMC. Finally, the pressure drop in microchannels with ribs is higher than in the SMC configuration.

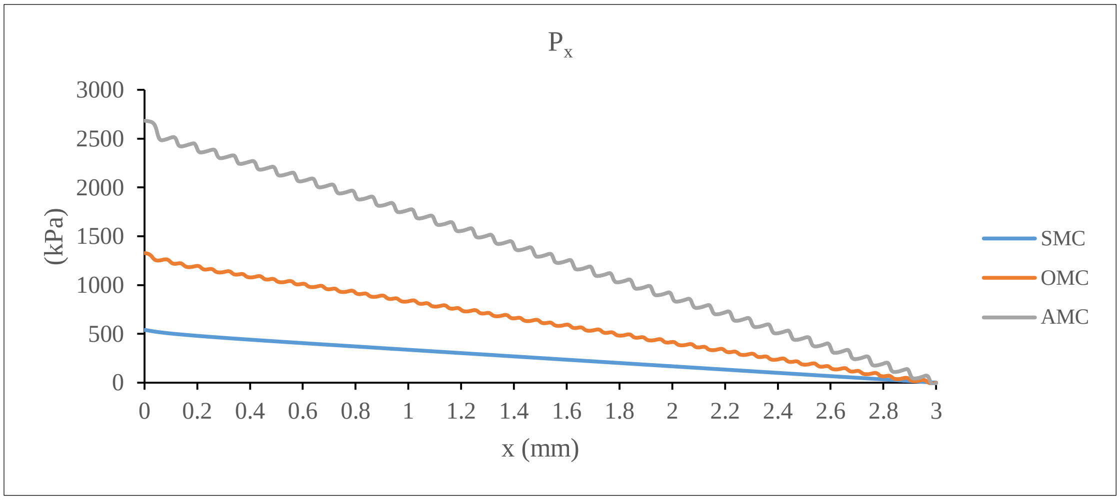

Figure-17:Flow pressure in x-direction Re=400.

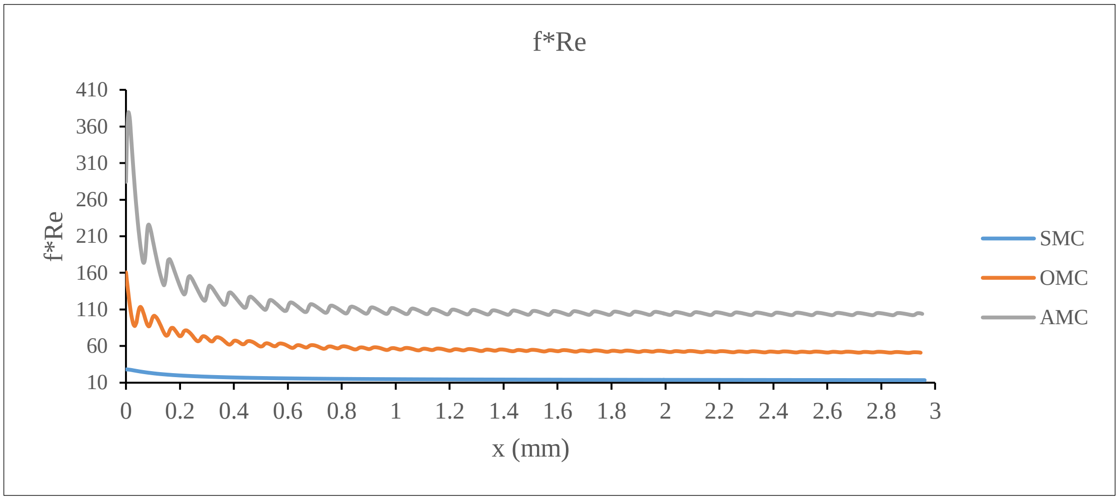

Figure-18: Local friction factor in x-direction Re=400.

Analyzing the behavior of the local friction factor along the microchannels (Figure-18). In the inlet of the channel, the local friction factor is larger compared with rest of the values along the channel, which corresponds to the hydrodynamic developing region, however, the local friction factor rapidly decreases along the flow direction. When the flow has reached the hydrodynamic developed condition, the local friction factor tends to a constant value. The triangular ribs lead to oscillation in the local friction factor along the microchannel, specially, in the developing region, however, the magnitude of the oscillations declines in the developed region of the flow and its value continues decreasing very slowly, which could be explained by the increase of the microchannel length or even by the decrease of the viscous effects caused by the increment of the temperature along the channel. The reason of the oscillation in the local friction factor is explained by the constant contractions and expansions that the flow suffers along the microchannels with ribs, being higher in the AMC configuration than in OMC, due to a larger pressure variation between the contractions and expansion of the flow passage, as was explained before. On other hand, with respect to the average friction factor (Figure-19), this declines when Re increases, where the decrease is strong between Re=100 to 300 and more slightly between Re 300 to 400. The AMC configuration has the higher values of average friction factor followed by the OMC and finally the SMC configuration has the minimum values of average friction factor for all range of Reynolds considered. Figure-20 shows the average friction factor normalized with respect to the smooth microchannel ($\bar{f}/\bar{f}_o$). The AMC configuration has the greatest increment than the OMC configuration, also, $\bar{f}/\bar{f}_o$ increases with a higher slope in microchannels with aligned ribs than the microchannel with offset ribs. The average friction factor in the microchannels with aligned rib distribution is 3.17 times at Re=100 & 4.72 times higher with respect to the smooth microchannel, on the other hand the $\bar{f}/\bar{f}_o$ in the OMC configuration is 1.8 to 2.3 times greater compared with smooth microchannel.

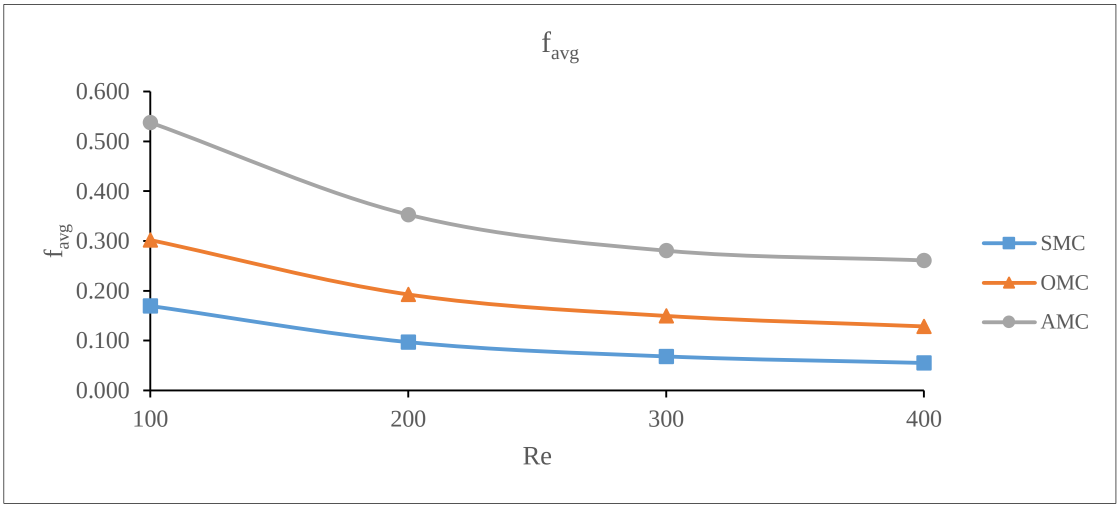

Figure-19: Average friction factor.

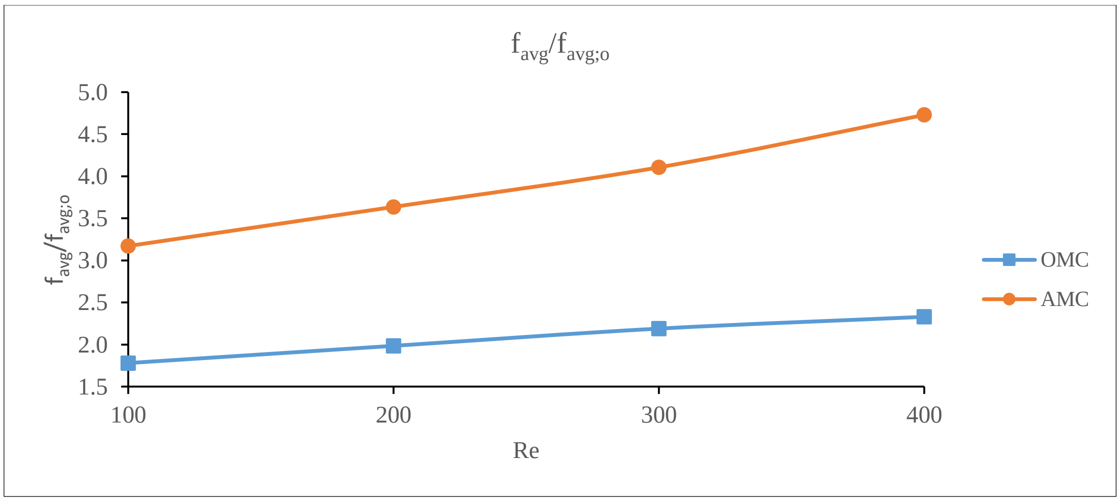

Figure-20: Variation of f_{avg}/f_{avg} with Re.

8.2.3.-Heat transfer

The ribs have a great impact in the heat transfer performance of the heat sink. The Temperature distribution of the microchannels with and without ribs are shown below (Figure-21). It can be seen that a higher Reynolds number implies a better heat transfer performance, independently of the geometry of the heat sinks evaluated. For the SMC, a pronounced temperature gradient occurs in the y-direction, where the temperature in the channel center is lower, and the wall temperature along the SMC is higher. The use of the triangular ribs favors a lower temperature gradient in y-direction, due to the mixture between the cold water from the microchannel center and hot water near sidewalls, which is generated by chaotic advection behind the ribs. The presence of the ribs causes a noticeable decrease in the wall temperature along the microchannel, also, the ribs imply an increases of the total heat transfer area between the fluid and the solid which favors to reduce the global thermal resistance. The thermal boundary layer is broken up periodically by the ribs and the length to redevelop the thermal boundary layer increases with the Reynolds number, however, this effect increases the thermal performance, allowing a better mixture of the fluid inside the microchannel. As mentioned before, low Reynolds number could generated laminar stagnation in the upstream of the ribs, which deteriorates the heat transfer performance.

For the multi-junction solar cell, the upper surface temperature of the microchannel is an important parameter because through this temperature is possible to determine the temperature of the multi-junction solar cell, considering an unidirectional heat flow due to only heat conduction. Based on Figure-22, for all the configuration analyzed, the average temperature of the upper surface ($\bar{T}_{w;MCHS}$) of the microchannel is lower than 300 K, being SMC configuration with the highest average temperature, and the AMC with the lowest $\bar{T}_{w;MCHS}$. The behavior of $\bar{T}_{w;MCHS}$ with respect to Re corresponds to a strong decline as Reynolds increases between 100 to 300, and more slightly when Re is higher than 300, even, it is seeming that Re over 400 the behavior of $\bar{T}_{w;MCHS}$ tends to be constant. With respect to the local Nusselt number (Nu_x), in the thermal developing region Nu_x has its highest values and it decreases rapidly to a constant value in the thermal developed region (Figure-23), similarly to the local friction factor, however, in this case the oscillation of the Nusselt number is related with fluctuation of the fluid temperature generated by the contraction and expansion of the flow along the channel. The AMC configuration generated highest values of local Nusselt number and the smooth microchannel has the lowest values. With respect to the average Nusselt number (Figure-24), it increases as Re increments from 100 to 300, however, for Re values higher than 300 the raise is slightly, and tends to a constant value for the smooth microchannel. It has been shown that an aligned distribution of the microchannel generates higher thermal performance than the offset arrangement, as well as the pressure drop is higher in the microchannel with aligned ribs, which is an important issue to consider. Normalizing the Nusselt number (Figure-25) of the microchannels with ribs, with respect to the smooth microchannel (Nu_o). It is possible to quantify the increase generated by the ribs in two dispositions analyzed. The microchannel with offset ribs distribution increases the Nusselt number slightly and almost linearly between 1.5 to 1.8 times, on the other hand, for the microchannel with aligned ribs distribution in general the Nu/Nu_o is greater than the offset ribs distribution, being 1.85 to 1.94 times greater, but in this case the behavior of Nu / Nu_o does not correspond to a sustained increase, since for Re= 200 a decrease in its value is generated, which could be explained since Nusselt number in the smooth microchannel has its greater increase between Re= 100 and 200, however, for Re over 300 the Nusselt diminishes its slope and tends to a constant value.

Finally, we ca summarize the principal aspects related with microchannels using forward triangular ribs:

a) The increase of the heat transfer area owing to the presence of ribs leads to a heat transfer enhancement.

b) The throttling effect caused by the sudden contractions and expansions of the cross-section induce to accelerate the flow.

c) The ribs broken up the hydraulic and thermal boundary layer periodically. The redevelopment depends of the Reynolds number, where for high Re in the AMC configuration the length for reattachment of the boundary layers is higher than the length between ribs.

d) For low Re, small laminar stagnation zone in the upstream of the ribs would appear, but at high Re this condition disappear.

e) Vortexes generated behind ribs lead to chaotic mixing between cold water in microchannel center and hot water near sidewalls.

f) The increment of Re introduces an improvement of the heat transfer performance, but it is accompanied by an increment of the pressure drop along the microchannel.

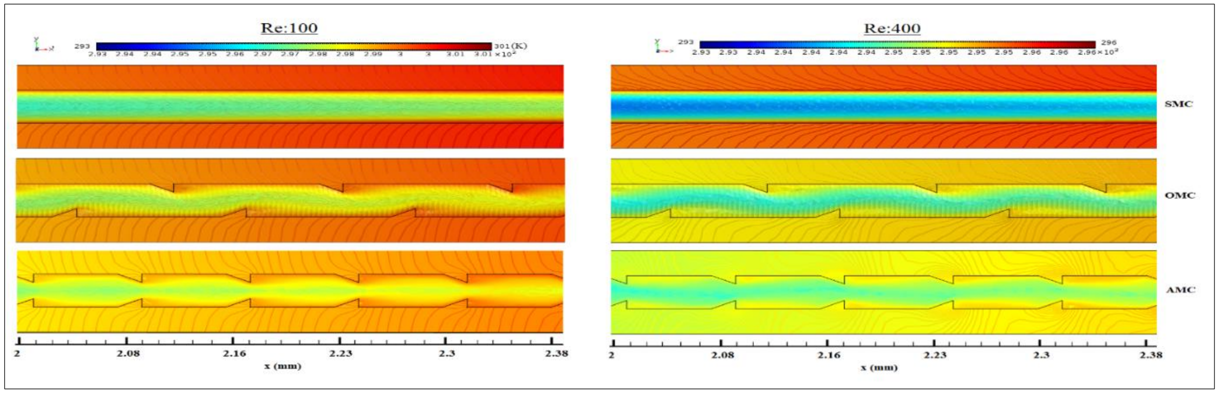

Figure-21: Temperature distribution in the microchannels at Re=100 & 400 (plane x-y; z=H/2)

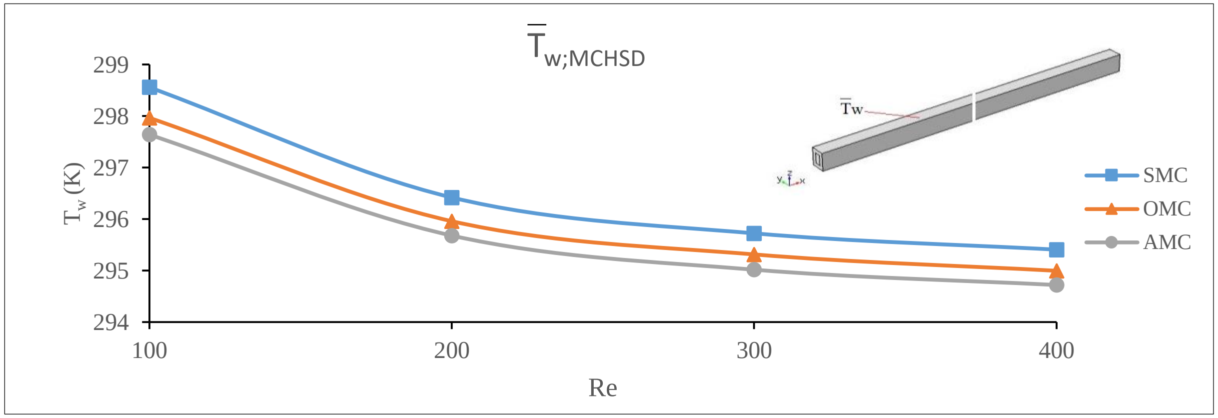

Figure-22: Average wall temperature of the microchannel (z=H)

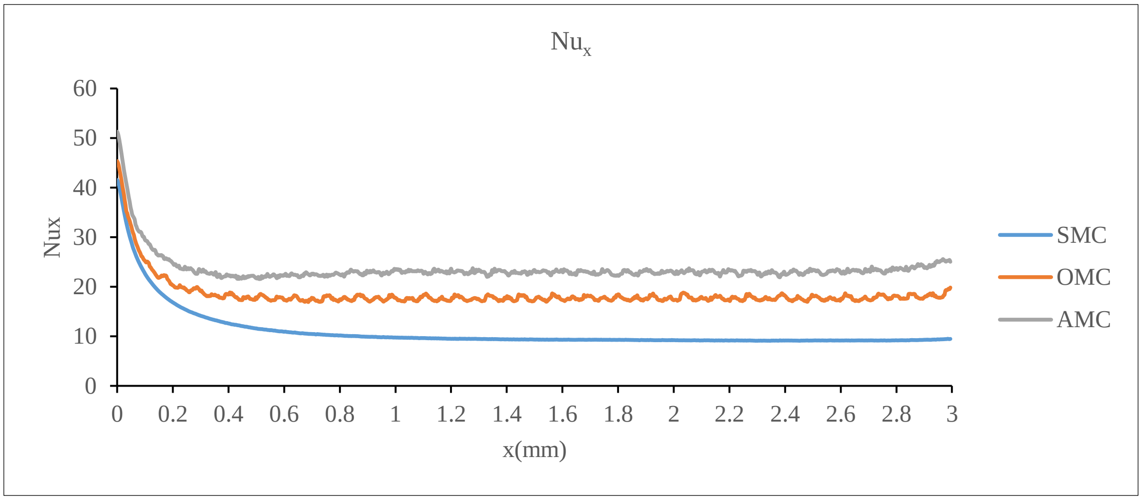

Figure-23: Local Nusselt number in x-direction Re=400.

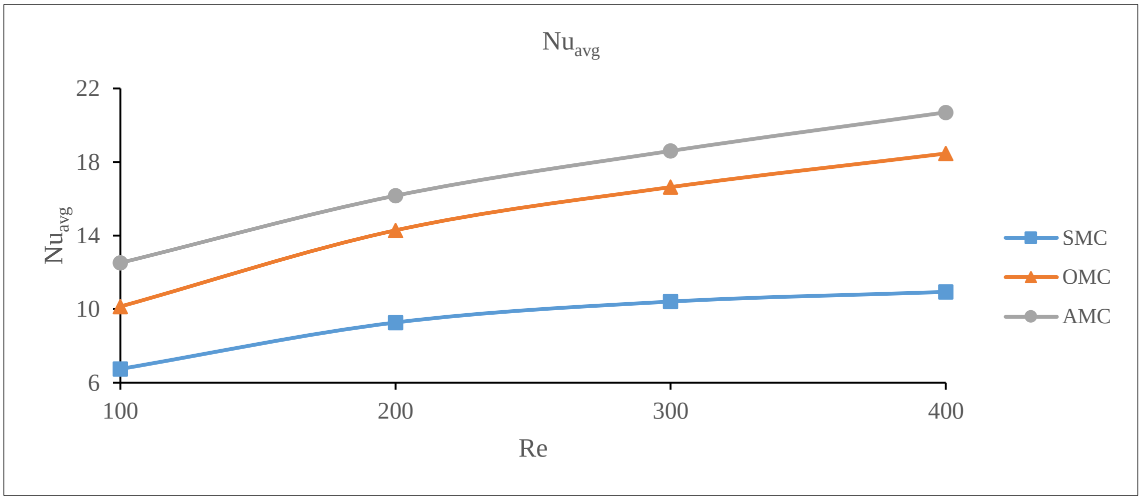

Figure-24: Average Nusselt number.

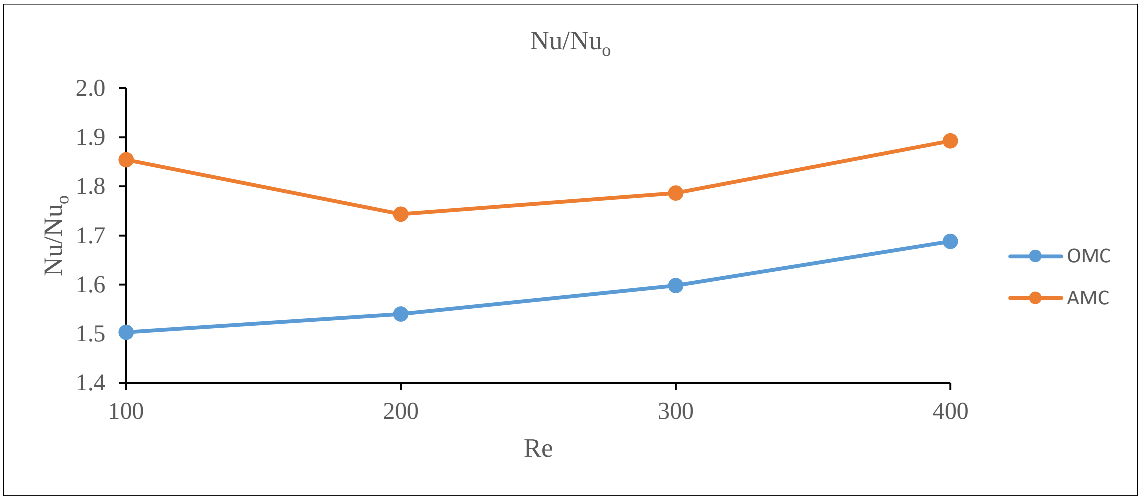

Figure-25: Variation of Nu/Nuo with Re.

8.2.4.-Global thermal resistance and pumping power in the MCHSD.

As was mentioned, a microchannel heat sink device (MCHSD), with 30 parallel microchannels with triangular ribs has been proposed and analyzed as cooling system of a multi-junction cells subjected to high solar concentration levels. Based on the flow parallel distribution proposed in the MCHSD, we assume that total pressure drop is equivalent to the pressure drop of each microchannel multiplied by the total number of parallel channels that conform the MCHSD, we neglect any drop pressure that can be caused by a manifold in the inlet and outlet of the MCHSD. Then Eq-39 was used to determine the total pumping power of the MCHSD. As well as, insulation boundary was considering in the y-direction of the microchannel domain, which means that there is no thermal interference between channels, therefore the global thermal resistance (m^2K/W) determined in the simulations (Eq-40) represents the global thermal resistance of the MCHSD system $(R_{th,MCHSD})$. Figure-26 & Figure-27 show the behavior of $R_{th,MCHSD}$ and the total pumping power ($W_{p,MCHSD}$) with respect to Reynolds number, where based on the data below, it is important to note that at low Reynolds range (100-300) the global thermal resistance drops faster, otherwise, when Re> 300 the global thermal resistance declines slowly and tends to be constant. On the other hand, the pumping power increases exponential with respect to Re for the three cases analyzed. As was expected, the MCHSD with smooth microchannels has the highest global thermal resistance and the minimum pumping power requirement, on the other hand, the MCHSD with aligned ribs has the minimum global thermal resistance for all range of Re evaluated and the maximum pumping power demand. MCHSD with triangular ribs has a higher heat transfer area and generates greater convective coefficient, therefore it is expected to have lower thermal resistance in this cases, however, as explained before, the microchannels with forward triangular ribs have a greater pressure drop, due to the continuum expansion and contraction of the flow, change in the flow direction, and acceleration by the reduction of the cross section.

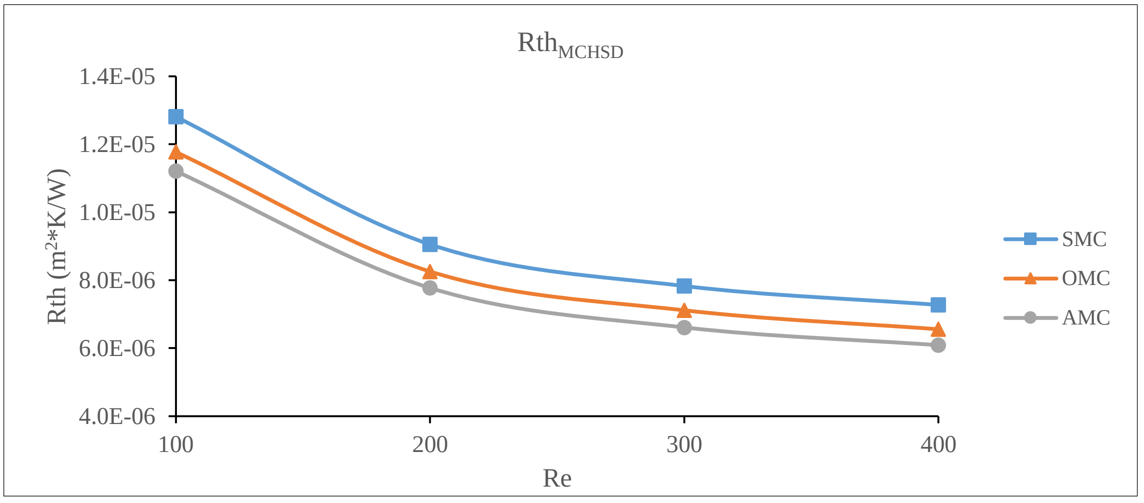

Figure-26: Global thermal resistance of MCHSDs.

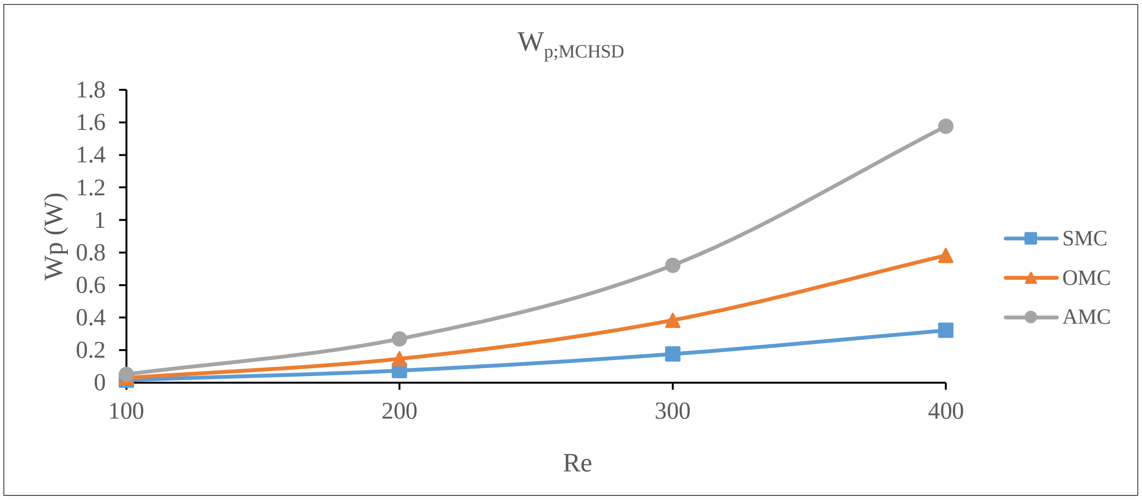

Figure-27: Pumping power of MCHSDs.

8.2.5.-HCPV with MCHSD.

A MCHSD has been proposed to be integrated in direct contact to a multi-junction solar cell subjected to a high concentration level (Figure-3). The goal is to control and keep the solar cell temperature in a low ranges with a maximum effective solar cell power generation (P_e). MCHSD with forward triangular ribs can keep and control the solar cell temperature in a very low range (T_{SC}), compared with a FPHS passive cooling system. Nonetheless, Figure-28 shows that at Re=400 the pumping power demand can achieve the 10% and 45% of the total solar cell power generated, when MCHSD considers SMC and AMC, respectively. MCHSD with forward triangular ribs demand higher percentage of power, being the AMC configuration the worse in this aspect than OMC, so then the P_e suffers an important reduction due to the pumping power requirement by the MCHSD with forward triangular ribs.

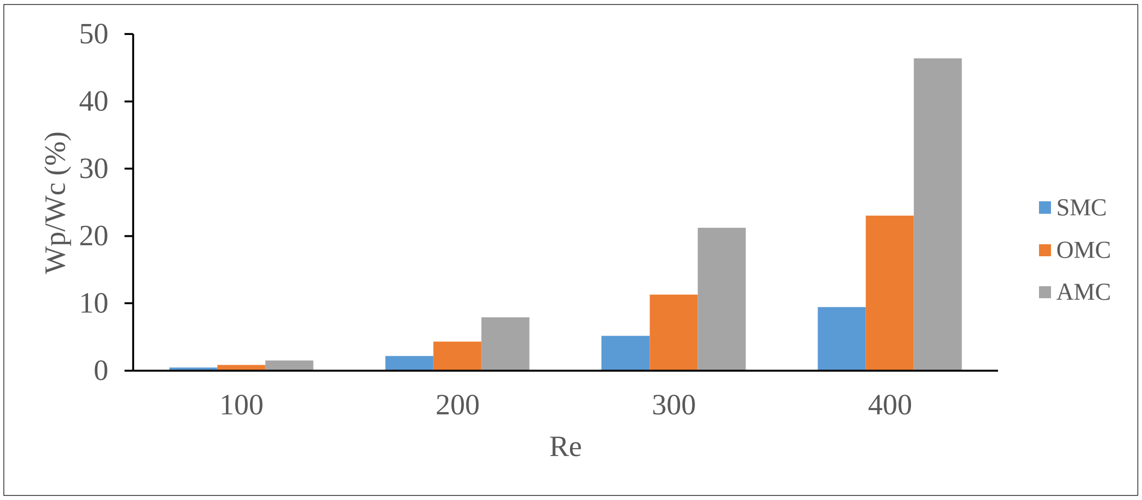

Figure-28. Percentage of pumping power over solar cell power (W_p/W_{sc}).

Figure-29 shows the behavior of P_e (Eq-36) with respect to Re. Note that at Re=100 the P_e achieves its maximum value for all the three MCHSD configurations and the percentage difference among the three configurations is minimum (Figure-28), where the P_e in the MCHSD-AMC has a reduction of 1.5%, MCHSD-OMC of 0.8%, and the MCHSD-SMC of 0.5%, with respect to the solar cell power. The MCHSD-SMC has the greatest P_e value for all the Re range, where P_e= 3.4 & 3.1 (W) at Re=100 and 400, respectively. On the other hand, P_e in the MCHSD-AMC suffers the sharpest decreases as Re increases, being P_e= 3.34 & 1.8 (W) at Re=100 & 400, respectively, due to the high increment in the pumping power and the complex geometric feature proposed. Finally the MCHSD-OMC has a higher decreases in the P_e than the MCHSD-SMC, but its complex geometric configuration affect in a lower magnitude the reduction of the effective solar power, being its maximum reduction equivalent to 22% between Re 100 and 400.

Figure-30 shows the solar cell temperature (Eq-37) with respect to Re. As Re increases the solar cell temperature decreases, being lower than 301 K for all the three configuration considered in the MCHSD (SMC, OMC, and AMC). The MCHSD-SMC generates the greatest global thermal resistance of the whole system, therefore, the highest solar cell temperature occurs using this type of channel geometry, with temperatures of 300.5 K and 297.3 K when Re=100 & 400, respectively. In the case of the MCHSD-AMC, that produces the lowest global thermal resistance, the solar cell temperature is equal to 299.5 K at Re=100 and 296.6 K at Re=400, which corresponds on average a temperature difference of 0.75 K with the MCHSD-SMC for all the evaluated Re range. The solar cell temperature is lower in MCHSD-OMC than in MCHSD-SMC, but the difference is not higher than 0.45 K on average. The solar cell temperatures achieved with the OMC configuration are 299.9 K and 296.9 for Re=100 & 400, respectively. Note that when Re<200, the T_{SC} decreases heavy, however, at Re>200 it decreases slightly and tends to a constant value.

The lower thermal limit of the solar cell cooled by MCHSD is bounded by the inlet coolant temperature. Consistently with the previous statement, we have determined that the solar cell temperature increases less than 7.5 K with SMC at Re=100 and even less than 5.5 K for all MCHSD scenarios analyzed with Re$\geq$ 200. Thus, the effect of solar cell temperature on the cell´s efficiency is very small for all practical purposes, and therefore the temperature change of the solar cell can be considered negligible when compared to the large temperature increase that is produced in a flat plate heat sink and its large effect on the efficiency.

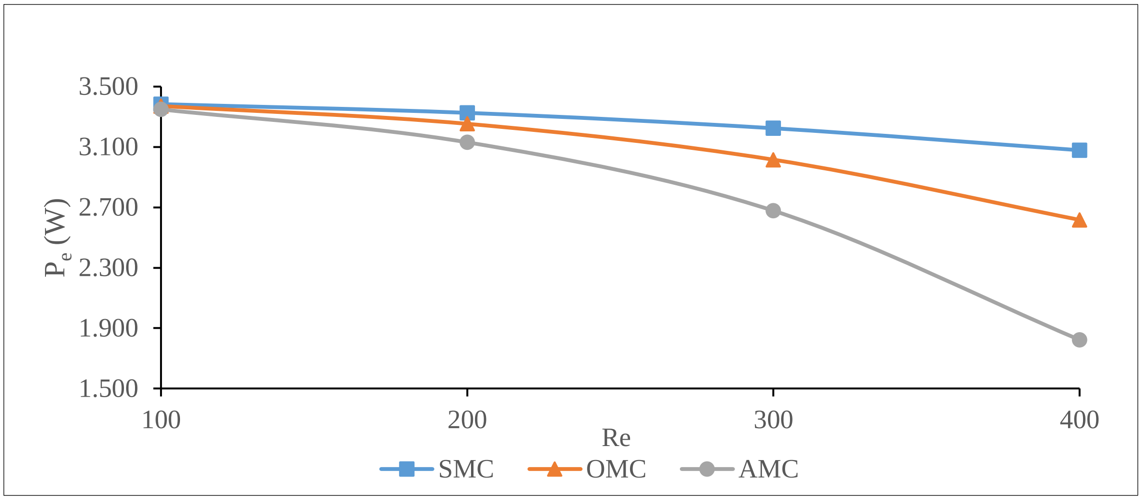

Figure-29. Effective solar cell power (P_e) under different Reynolds numbers.

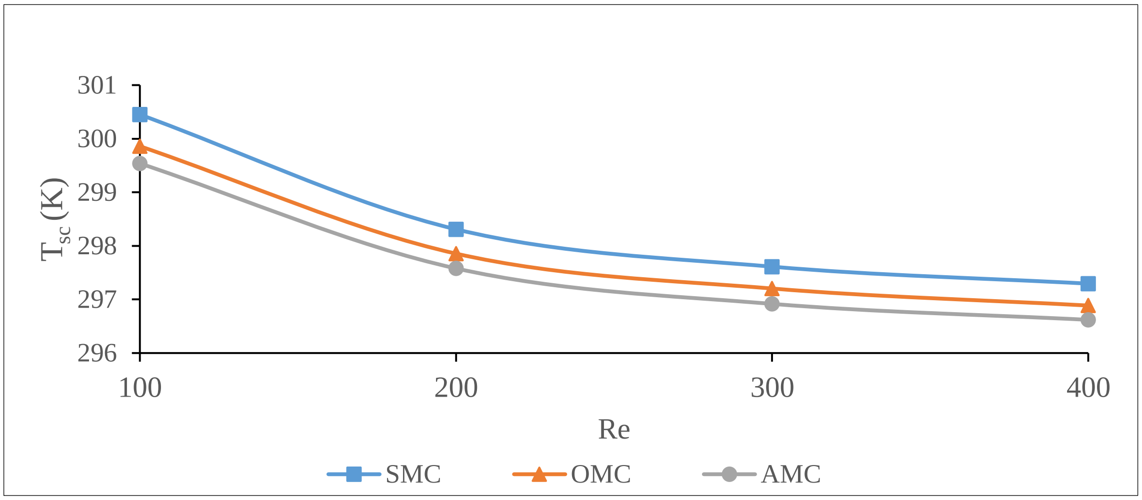

Figure-30. Solar cell temperature (T_{sc}) under different Reynolds numbers.

8.3.-Further practical comments

The present study analyzed a MCHSD with complex internal geometries as cooling system for HCPV technology, which is compared with a flat plate heat sink passive cooling. Based on the above results we can insure that a MCHSD shaped by 30 parallel channel with forward triangular ribs, being an integral component of the architecture of the multi-junction solar cell, can control and keep in a very low range the solar cell temperature (<301 K) with a very low thermal resistance, however, the pumping power generated by the pressure losses across the microchannel has negative effect on the effective power generated by the solar cell. A MCHSD with forward triangular ribs (AMC and OMC) enhances the cooling capability of multi-junction solar cell with respect to MCHSD with SMC, however, the effective solar power suffers a significantly reduction when Re>200 in the MCHD with ribs, for example, the effective solar power is reduced 23% and 46% when Re=400 due to the pumping power demand in the MCHSD-OMC and MCHSD-AMC, respectively, therefore, it is necessary to establish a point where forward triangular ribs favor to reduce the solar cell temperature with an acceptable pumping power demand. The greatest solar cell temperatures are reached with MCHSD-SMC, but the temperatures achieved with this channel geometrical configuration are not higher than 0.75 K and 0.45 K on average, with respect to the MCHSD-AMC and MCHSD-OMC. If we considered a pumping power demand should not be longer than 10% of the effective solar power, the MCHSD with forward triangular ribs are more recommended to be used with Re≤200, whereas, MCHSD-SMC arises as a better solution when Re>300. The below table (Table-3) summarizes the principal parameters that have been mentioned and analyzed above of the three microchannel configuration analyzed, with the intention to present the result in a practical way to researcher and developers. Table-3 resumes the global thermal resistance R_{thg}, pumping power Wp, solar cell temperature T_{sc} achieved, ΔT between the solar cell and the inlet coolant temperature, and the effective power Pe of the whole system.

Table-3: Principal parameter of the ensemble MCHSD-Solar cell.

Re	Configuration	R_{thg} (m^2*K/W)	Wp (W)	T_{sc} (K)	ΔT (K)	Pe (W)
100	SMC	1.28x10^{-5}	0.02	300.45	7.45	3.38
	OMC	1.18x10^{-5}	0.03	299.86	6.86	3.37
	AMC	1.12x10^{-5}	0.05	299.54	6.54	3.35
200	SMC	9.05x10^{-6}	0.07	298.31	5.31	3.33
	OMC	8.26x10^{-6}	0.15	297.86	4.86	3.25
	AMC	7.77x10^{-6}	0.27	297.58	4.58	3.13
300	SMC	7.83x10^{-6}	0.18	297.61	4.61	3.2
	OMC	7.11x10^{-6}	0.38	297.20	4.20	3.0
	AMC	6.61x10^{-6}	0.72	296.92	3.92	2.7
400	SMC	7.27x10^{-6}	0.32	297.30	4.30	3.1
	OMC	6.56x10^{-6}	0.78	296.89	3.89	2.6
	AMC	6.09x10^{-6}	1.61	296.62	3.62	1.8

An important point to highlight corresponds that the minimum solar cell temperature achieved using the FPHS with the highest heat transfer area (FPHS-C) corresponds to 324 (K) and 354 (K) when T_{surr}=298 (K) & 328 (K), respectively (Figure-13). On the other hand, for any MCHSD configuration analyzed (SMC, OMC, AMC), the solar cell temperature achieved is lower than 301 K. Hence, the passive cooling system analyzed is not an effective way to control the solar cell temperature for high level of suns concentration (CF=1000), even it has a high dependency of the surrounding temperature, which makes even more difficult to control the solar cell temperature. While, the results show that the MCHSD proposed in this study has a very good control performance controlling the solar cell temperature for a CR=1000 without dependency of surrounding temperature, and even the heat transfer area required in the MCHSD is just the same than the solar cell, allowing to have a compact and lightweight system. Nonetheless, the passive cooling analyzed does not demand electrical power to operate, but as was mentioned for high concentration level (1000 suns) this system does not assure a lower and safe solar cell temperature, as the MCHSD can do. In addition, the overheating achieved by the multi-junction solar cell using a FPHS reduces more the useful electrical power than the MCHSD generates due to the pumping power demand.

The literature has mentioned that the best cooling systems for HCPV technology are microchannel heat sink, jet impingement, and liquid immersion. Based on the work developed by Sanjeev et al. [34], we compare (Table-4) our proposed cooling system with the other two cooling option highlighted. In the same line, microchannel heat sink presents a very low thermal resistance with small heat transfer area, being suitable for high concentration levels and small multi-junction solar cells, but a high pressure drop occurs along the microchannel that demands large pumping power. On the other hand, liquid immersion cooling system allows to transfer the heat form all surface of the solar cell, which favor having a uniform temperature, however, salt deposition occurs being a problem as well as a more complicated system design is normally needed. Finally, jet impingement cooling option presents a very low thermal resistance but is necessary develop a suitable design of the system, due to disturbances occurs when water from one jet meets the water from neighboring jet, which affect the heat transfer capability. [35].

Table-4: Comparative active cooling technologies for HCPV.

Type of cooling	**Solar cell**	**CF**	**T_{sc} (K)**	**Flow condition**	**R_{thg} (m^2*K/W)**	**Author**
Jet Impingement	Silicon	500	313	Not Reported	Not Reported	Royne et al. [4]
	Dummy SC	300-500	-	0.049 kg/s	5.9×10^{-5}	Barrau et al. [35]
Liquid Immersion	Multi-junction	50	344-423	0.00138 kg/s	Not Reported	Xin et al. [36]
	Silicon cell	250	318	Not Reported	3.3×10^{-4}	Zhu et al. [37]
	Silicon cell	250	323	2.23 m3/h	1.7×10^{-4}	Zhu et al. [38]
	Silicon cell	9	293-304	Not Reported	1.1×10^{-3}	Sun et al. [39]
MCHSD-SMC	Multi-junction	1000	297.3-301	Re=100-400	9.2×10^{-6} $_{(avg)}$	Present study
MCHSD-OMC			297-300		$8.4 \times 10^{-6}$$_{(avg)}$	
MCHSD-AMC			296.6-299.5		$7.9 \times 10^{-6}$$_{(avg)}$	

9. CONCLUSION REMARKS.

A Computational Fluid Dynamics and heat Transfer analysis has been carried out to evaluate a microchannel heat sink device (MCHSD) with and without forward triangular ribs installed on the inner sidewalls of the channels as cooling system in a HPCV arrangement. Aligned and offset distributions of the ribs have been studied in detailed with respect to the friction factor, pumping power, Nusselt number and global thermal resistance for laminar flows. A thermal analysis of a typical HCPV-based flat plate heat sink (FPHS) cooling system has been developed to compare the thermal performance of MCHSD against the former one. From the present work, the following conclusions can be drawn:

- A flat plate heat sink (FPHS) as cooling system in HCPV has difficulties to control the solar cell temperature, because its high dependency on the surrounding temperature. An increase of the T_{surr} reduces the effectiveness of the cooling system, which corresponds to a higher overheating in the solar cell. Although, the FPHS system does not demand mechanical work or electrical power to its operation because operate under surrounding conditions, it is not recommended for high sunlight concentration levels.
- The FPHS-C achieves minimum solar cell temperature equal to 324 K when $T_{surr} = 298$ K. On the other hand, the FPHS-A has the lowest heat transfer area, therefore, it generates a minimum solar cell temperature over 373 K, which corresponds to an unsafe temperature condition for the solar cell. While larger the heat transfer area of the FPHS is, lower is the solar cell temperature, and more weight is added to the whole HCPV system.

- Forward triangular ribs enhance the heat transfer capability and increases the pressure drop with respect to a smooth microchannel. The simulation results shown that microchannels with aligned and offset rib distribution increase 1.8 times and 1.6 times on average the Nusselt number, respectively, compared with SMC. However, the average friction factor is 3.9 and 2.3 time on average greater for a microchannel with aligned and offset ribs distribution than SMC, respectively.
- The principal aspects that enhance the heat transfer performance of microchannel using forward triangular ribs, considering aligned and offset distribution can be summarized as: (1) an increase of the heat transfer area due to the ribs; (2) The throttling effect caused by the sudden contractions and expansions of the cross-section induces to accelerate the flow; (3) The ribs broken up the hydraulic and thermal boundary layer periodically. The redevelopment length depends on the Reynolds number, where for high Re in the AMC configuration the length for reattachment of the boundary layers is higher than the length between ribs; (4) the vortexes generated behind the ribs lead to a chaotic mixing between the cold water in microchannel center and the hot water near the sidewalls.
- A MCHSD integrated in direct contact with the multi-junction solar cell can reduce and control significantly the temperature of the solar cell, since the only thermal fence between the MCHSD and the multi-junction solar cell corresponds to the own thermal conductive resistance of the solar cell. The use of microchannels as heat sink can reduce the weight and of the system and reach a high heat transfer coefficient on small area compared with a passive cooling system that requests a

greater heat transfer area to refrigerate solar cell. The solar cell temperature reached with the MCHSD is lower than 301 K, enabling to operate the solar cell under a maximum efficiency condition.

- MCHSD with forward triangular ribs loses its advantage as an effective and efficient cooling system for HCPV application as Re increases, due to the pumping power demand in AMC and OMC configurations, which is significantly greater at Re>200. MCHSD-SMC rises as better option at Re≥300, since it can control the solar cell temperature in a low range with a pumping power demand lower than 5.2% and 9.5% of the power produced by the solar cell at Re= 300 & 400, respectively, unlike the microchannel heat sink with triangular ribs, where pumping power achieves by 41% and 23% of the total power generated by the multi-junction solar cell in the aligned and offset rib distribution, respectively, smooth microchannels-based heat sinks are better in terms of pumping power at Re≥300.
- Compared with a flat plate heat sink, the MCHSD can control better the solar cell temperature and keep it in a lower range. The MCHSD can reduce the solar cell temperature at least in 23 K compared with FPHS-C when T_{surr}=298 K and 52 K when T_{surr}=328 K. Nevertheless, the principal advantage that the passive cooling has, compared with the MCHSD, is the null power consumption. However, the temperatures achieved with the FPHS would significantly reduce significant the conversion efficiency.

- The integration of the MCHSD on a HCPV has been proposed to be carried out in the manufacturing process of the solar cell. Future analysis and studies can investigate this integration, as well as other flow structures. Incorporating a MCHSD as cooling system in HCPV can keeping the solar cell temperature for a high sun level concentration in low range.
- Based on the simulations results, the inlet pressure reached in the microchannels with forward triangular ribs could be impractical for the material considered in the microchannels, especially for the microchannels with aligned ribs distribution, because if its relatively high inlet pressure.
- The numerical results reported in this article can be very useful for researchers and developers that are currently investigating and developing new integrated cooling devices based on microchannels, since our results demonstrated that by integrating complex geometrical features to microchannel walls, a better control of the solar cell temperature maximizing P_e, and minimizing global thermal resistance in HCPV can be achieved.

REFERENCES

Leonardo Micheli, Eduardo F. Fernández, Performance, limits and economic perspectives for passive cooling of High Concentrator Photovoltaics, Solar Energy Materials & Solar Cells153(2016)164–178. [1]

Kinsey GS, Edmondson KM. Solar Cells 2009:279–88. [2]

Leonardo Micheli, Tapas Mallick. Opportunities and challenges in micro- and nano-technologies for concentrating photovoltaic cooling: A Review. Renewable and Sustainable Energy Reviews. 2013. [3]

A. Royne, C.J Dey, D.R Mills. Cooling of photovoltaic cells under concentrated illumination a critical review. *Solar Energy Materials and Solar Cells Journal*. 2005; 451-483. [4]

Ali Radwan, Mahmoud Ahmed. Analysis and simulation of concentrating photovoltaic systems with a microchannel heat sink. Solar Energy. 2016. [5]

Ali Radwan, Mahmoud Ahmed. The influence of microchannel heat sink configurations on the performance of low concentrator photovoltaic systems. Applied Energy. 2017. [6]

Leonardo Micheli, Tapas Mallick. Opportunities and challenges in micro- and nano-technologies for concentrating photovoltaic cooling: A Review. Renewable and Sustainable Energy Reviews. 2013. [7]

D.B Tuckerman and R. Pease. High performance heat sinking for VLSI. IEEE Electron Devise Letters.1981; 126-129. [8]

Ali Radwan, Mahmoud Ahmed. The influence of microchannel heat sink configurations on the performance of low concentrator photovoltaic systems. Applied Energy. 2017. [9]

Ali Radwan, Mahmoud Ahmed. Analysis and simulation of concentrating photovoltaic systems with a microchannel heat sink. Solar Energy. 2016. [10]

Rahimi (Rahimi, M., Karimi, E., Asadi, M., Valeh-e-Sheyda, P., 2013. Heat transfer augmentation in a hybrid microchannel solar cell.
Int. Commun. Heat Mass Tranf. [11]

Reddy, K.S., Lokeswaran, S., Agarwal, P., Mallick, T.K., 2014. Numerical investigation of micro-channel based active module cooling for solar CPV system. Energy Proced. 54, 400–416. [12]

Ramos-Alvarado, B., Li, P., Liu, H., Hernandez-Guerrero, A., 2011. CFD study of liquid-cooled heat sinks with microchannel flow field configurations for electronics, fuel cells, and concentrated solar cells. Appl. Therm. Eng. 2494–2507. [13]

Agrawal, S., Tiwari, A., 2011a. Experimental validation of glazed hybrid microchannel solar cell thermal tile. Sol. Energy 85, 3046–3056. [14]

Kermani E, Dessiatoun S,Shooshtari A,Ohadi MM. Experimental investigation of heat transfer performance of a manifold microchannel heat sink for cooling of concentrated solar cells. Proceedings of the 59th Electronic Components Technol. Conference. 2009. [15]

Woei-Chong Tan, Kok-Keong Chong, Ming-Hui Tan. Performance study of water-cooled multiple-channel heat sinks in the application of ultra-high concentrator photovoltaic system. Solar Energy 147 (2017) 314–327. [16]

Nor Azwadi Che Sidik, Muhammad Noor Afiq Witri Muhamada, Wan Mohd Arif Aziz Japar, Zainudin A. Rasid. An overview of passive techniques for heat transfer augmentation in microchannel heat sink. International Communications in Heat and Mass Transfer 88 (2017) 74–83. [17]

Lei Chai, Guo Dong Xia, Hua Sheng Wang. Parametric study on thermal and hydraulic characteristics of laminar flow in microchannel heat sink with fan-shaped ribs on sidewalls. Part-1. International Journal of Heat and Mass Transfer. 2016. [18]

Kok-Cheong Wong, Jian-Hong Lee. Investigation of thermal performance of microchannel heat sink with triangular ribs in the transverse microchambers. International Communications in Heat and Mass Transfer 65 (2015) 103–110. [19]

Lei Chai, Guo Dong Xia, Hua Sheng Wang. Laminar flow and heat transfer characteristics of interrupted microchannel heat sink with ribs in the transverse microchambers. International Journal of Thermal Sciences 110 (2016)- [20]

Lei Chai, Guo Dong Xia, Hua ShengWang. Numerical study of laminar flow and heat transfer in microchannel heat sink with offset ribs on sidewalls. Applied Thermal Engineering 92 (2016) 32–41. [21]

Xie W, Dai Y, Wang R, Sumathy K. Concentrated solar energy applications using Fresnel lenses: a review. *Renewable Sustain Energy*. 2011; 2588–2606. [22]

F.P. Incropera, D.P. DeWitt, T.L. Bergman, A.S. Lavine, Fundamentals of Heat and Mass Transfer, Wiley, Hoboken, NJ, 2007. [23]

S. Kandlikar, W. Grande. Evolution of microchannel flow passages, Thermohydraulic performance and fabrication technology. ASME International Mechanical Engineering Congress & Exposition. 2002. [24]

T.J. Chung. Computational Fluid Dynamic book 4th Edition. 2009; 244-254. [25]

M.E. Steinke, S.G. Kandlikar, Single-phase liquid friction factors in microchannels, Int. J. Therm. Sci. 45 (2006) 1073–1083. [26]

Shah, R.K., & London, A.L. Laminar Flow Forced Convection in Ducts. London: Academic Press. 1978. [27]

H. Ghaedamini, P.S. Lee, C.J. Teo, Developing forced convection in converging–diverging microchannels, Int. J. Heat Mass Transfer 65 (2013) 491–499. [28]

G.D. Xia, Y.L. Zhai, Z.Z. Cui, Numerical investigation of thermal enhancement in a micro heat sink with fan-shaped reentrant cavities and internal ribs, Appl. Therm. Eng. 58 (2013) 52–60. [29]

APPENDIX

APPENDIX A: BASIC PRINCIPLES OF MULTI-JUNCTION SOLAR CELLS.

The light is composed by photons and when a light flux reaches onto a specific material, a fraction of the light flux is absorbed and transfers its energy to the electrons that are farthest from nucleus of the atom, which allows them to free themselves from the attraction of nucleus. The released electrons are susceptible to produce an electric current, if they are attracted immediately towards the outside. In steady state, the released electron (a) leaves a gap which translates into a positive charge. If this electron (a) is attracted to the outside, it will be an electron (b) from another neighboring atom that will fill the gap left, but it will generate a hole that must be filled by an electron (c) from another neighboring atom and so on. In this way an elementary charge circulation of electrons is generated in one direction, and holes (positive charge) in the opposite, which results in an electric current that is known as photoconductivity, which is specific to semiconductors. Depending on the material, there is a threshold of minimum energy (Eg) necessary to achieve the release of electrons by photons, which is known as band energy. Therefore, if the photon has an energy equal or greater than the bandgap; the electron will be released, nevertheless, if the photon has lesser energy that the bandgap; the electron would never be released. The energy that a photons has is related with its wavelength (λ), where higher energy implies a smaller wavelength, opposite case, lower energy implies bigger wavelength. In conclusion, the minimum energy to release the electron is function of the photon wavelength, for example, crystalline silicon has a band energy at 1.14 eV, so then photons that possess this energy requires a wavelength equivalent to 1.13 μm, however, the rest of photons absorbed by the material, but with lower energy and higher wavelength (λ) cannot be used for the photovoltaic conversion.

In solid-state physics, the valence band and conduction band are the bands that determine the electrical conductivity of the solid, therefore, electrons located in the valence band are those that are in the highest energy domain of the atom. On the other hand, those electrons that are in the conduction band, are those that have been extracted and free to circulate (note that the conduction band is empty when the material is not exposed to a photon flux). When a photon has sufficient energy, it is absorbed, making to pass an electron from the valence band to the conduction band, in the same way, if the photon has an energy greater than Eg, the photon generates the transfer of the electron, but the surplus energy is transformed into heat. A simple silicon solar cell corresponds to the union between P-type doped silicon plate (positive charge-doped with phosphorus atoms) and N-type silicon plate (negative charge doped with Boron), which is equivalent to a classical silicon diode, which subjected to a luminous radiation flow generates the release and transfer of electrons from the N-type plate to the P-type plate. The excess of electrons in the N-plate, subjected to the energy input of the photons, which is equal to or greater than the required Eg, allows the flow of electrons to the P-plate. With respect to multi-junction solar cells, these have highest efficiency, because the solar cell is conformed for multiple materials with bandgaps that span the solar spectrum. In other words, a multi-junction solar cells consists in single-junction solar cells stacked upon each other like a packet of different diodes connected in series, so then, each diode going from the top to the bottom has a smaller bandgap that the previous, and so it absorbs and converts the photons that have energies greater than the bandgap of that layer and less than the bandgap of the higher layer. Multi-junction solar cells have been studied since 1960, where in 1994 US National Renewable Energy Laboratory (NREL) broke the 30% barrier. The maximum efficiency reported by NREL correspond to 40.7%, which was achieved with a triple-junction solar cells. The maximum theoretical limit efficiency of multi-junction solar cells is 86.8%.

As was mentioned, the energy band of the material plays an important role in the conversion energy that occurs in a solar cell. With the intention of optimizing conversion efficiency of a photovoltaic cell, the solar cell should be able to absorb energy as much of the spectrum as possible, therefore, the bandgap of each material should cover a wide range. The election of the material to use in a multi-junction solar cell is completely related with the bandgap and the efficiency that is expected to achieve, where the principal materials used in multi-junction solar cells are GaInP (1.85 eV), GaAs (1.4 eV) and Ge (0.7 eV). Table-4 shows the efficiency and Eg values of single and multi-junction solar cells, considering different material and concentration sunlight, as well as, chart-1 shows how a multi-junction solar cell of GaInP/GaInAs/Ge harness much higher amounts of energy available in the solar spectrum than a silicon cell.

Table-5.Solar Cells Efficiency

Cell	# junction	Eff. %	Sun X	Eg1 (eV)	Eg2 (eV)	Eg3 (eV)
Si	1	25±0.5	1	1,14	-	-
GaAs	1	26,4±0.8	1	1,4		
Si	1	27,6±1	92	1,14	-	-
GaAs	1	29,1±1.3	117	1,4	-	-
GaInP/GaInAs/Ge	3	41,6±2.5	364	1,85	1,4	0,67

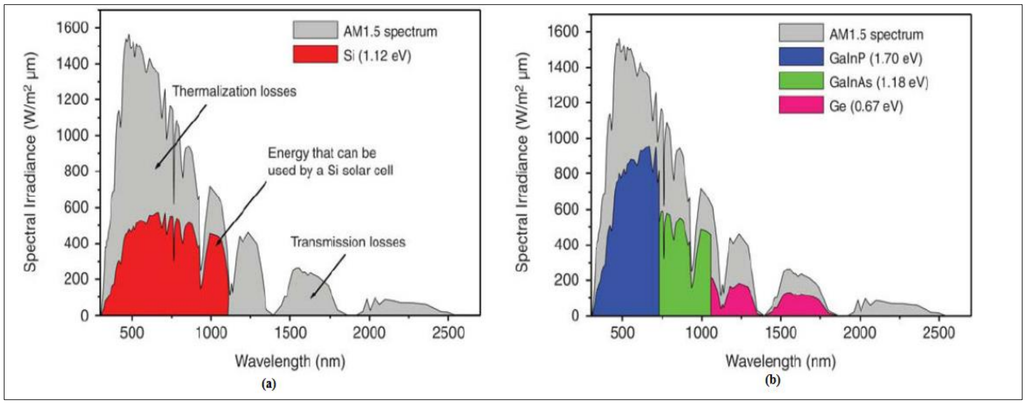

Figure-31: Conversion energy with respect to bandgap (AM-1.5), (a) Silicon cell, (b) GaInP/GaInAs/Ge cell

APPENDIX-B: COOLING SYSTEM IN HCPV BASED ON THE GEOMETRY.

As has been mentioned before, lens and mirrors are used to concentrate the DNI. If lenses are employed, the solar cells are normally placed underneath the light source, on the other hand, if mirrors are used, the cells are generally illuminated from below, this makes shading an important issue to consider in the design of the cooling system. The type of concentration system has an important relation with the cooling system required. Three types of geometric arrangements are proposed by Ref[2], which are: Point-Focus, Line-focus, and Larger point-focus geometric configuration.

- Point-focus geometric configuration (single cells): In this configuration, one concentrator system is used by a single solar cell. This system uses usually a fresnel lens. The cooling can be active or passive, however, if the heat sink is based on passive cooling, the area of the heat sink should be equal to the area of the solar cell with an amplified factor equivalent to the concentration level. For example, a heat sink of a solar cell under 50 times of concentration requires a passive cooling with an area equivalent to 50 times the area of the solar cell [3].
- Line-focus configuration: Normally uses parabolic mirrors or linear Fresnel lenses are used to focus the light over a row of cells. In this configuration, the solar cells have less area available for heat sinking, due to two of the cells sides are in close contact with neighboring cells.
- Larger-point focus configuration: The receptor consists in a multitude of densely packed cells and usually set slightly away from the focal plane to increase the illumination,

in addition, secondary concentrators may be used to improve the radiation flux. With respect to the cooling systems, Ref[2] mentions that densely packed modules have higher problems than the two other geometries, because only the back side of the cell can be used for integrating a cooling system (only the solar cells in the edge of the module have one lateral side free), which implies that passive cooling systems cannot be employed in high concentration levels.

- The transition between low and high CPV systems is related with concentration factor and the tracking used. Ref[30] gives the following classification that even defines the type of solar cells to use.

Table-6. CPV classification based on the concentration ratio Ref[30].

Class of CPV	Concentration ratio	Tracking	Type of solar cell
High concentration(HCPV)	300-1000	Two-axis	III-V multi-junction solar cell
Low concentration (LCPV)	<100	One or two-axis	c-Si or other cells

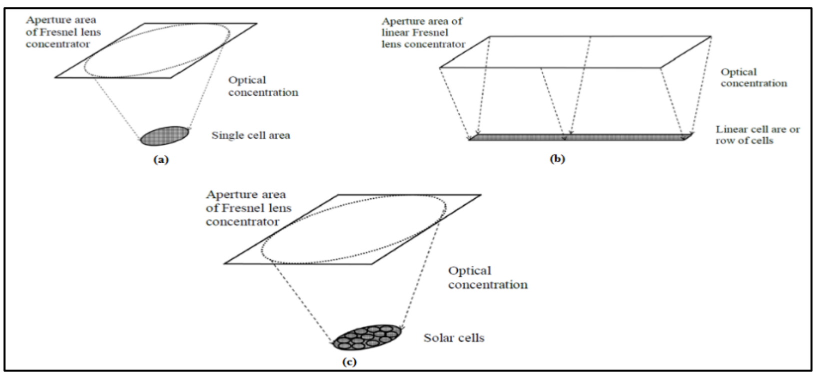

Figure-32: Concentration systems based on cooling system. (a) Point-focus, (b) Line-focus, (c) Larger-point focus. Ref[2].

APPENDIX C: FINITE ELEMENT METHOD

The numerical simulations are performed using COMSOL 5.1 software, which solves using the finite element method (FEM) the governing equations. To avoid unstable and inaccurate numerical issues, it is necessary to considerer the Galerkin test function "$\boldsymbol{\phi_N^e}$" plus numerical diffusion test functions "$\boldsymbol{\psi_N^e}$", where for steady problems the numerical scheme is:

$$(\phi_N^e + \psi_N^e; R) = \int_\Omega (\phi_N^e + \psi_N^e) * R d\Omega = 0$$

Where $\boldsymbol{R}$ is a residual function, which represents the difference between the numerical solution and the exact solution of each variable that we have in the governing equations. On the other hand, the numerical diffusion plays a role of numerical viscosity. The numerical stabilization employed by solving the governing equation is consistent numerical stabilization, specifically, streamline diffusion, which introduces numerical diffusion along the streamline direction providing numerical stability. However, as the convection become significant, it is not possible to eliminate entirely some numerical oscillation. Streamline diffusion is enough to obtain numerical solutions if the exact solution does not contain any discontinuities, therefore, in the boundary layer of the microchannel, streamline diffusion is not enough, because vorticities are generated due to the ribs. In other words, sharp gradients of velocity and temperature occur, hence, to handle this issue, crosswind diffusion is added, whose purpose is to dissipate numerical oscillation in boundary layer by adding diffusion orthogonal to the streamline direction. When numerical diffusion is employed, the Generalized Petrov-Galerkin (GPG) method is required to solve the differential governing equations.

With the intention of having a general view of the mathematical scheme of the GPG method, a brief development of the method is given with respect to reference:

$$\psi_N^e = \psi_N^{(a)} + \psi_N^{(b)}$$

$$\psi_N^{(a)} = \tau * u_i * \frac{\partial \phi_{N,i}^e}{\partial x_i} \quad (Streamline\ diffusion).$$

$$\psi_N^{(b)} = \tau^{(b)} * u_i * \frac{\partial \phi_{N,i}^e}{\partial x_i}\ (Crosswind\ diffusion).$$

Where τ is a numerical diffusion factor, that depends on the local Peclet number ($Pe_L = \frac{u*h}{2*\upsilon},\ \ h = mesh\ size, \upsilon = diffusion\ coefficient, u = convective\ term$), mesh size, and velocity components (u,v,w). The mathematical scheme by a convection-diffusion equation (Navier-Stoke and energy equation), which is solved through GPG method, is showed below considering the following residual function:

$$R_i = u_j * \frac{\partial u_i}{\partial x_j} - \upsilon \frac{\partial u_i}{\partial x_j \partial x_j} = 0$$

With respect to Eq-45 and integrating by part only with respect to the Galerkin test function (considering indicial notation):

$$\int_\Omega \left[(\phi_\alpha^e + \psi_\alpha^a) * \left(u_j \frac{\partial u_i}{\partial x_j} - \upsilon \frac{\partial u_i}{\partial x_j \partial x_j} \right) + \psi_\alpha^b u_j u_{i,j} \right] d\Omega = 0$$

$$\int_{\Omega} \left(u_j \phi_\alpha^e \phi_{B,j}^e u_{Bi} + \upsilon \phi_{\alpha,j}^e \phi_{B,j}^e u_{Bi}\right) d\Omega - \int_{\Gamma} \left(\phi_\alpha^* \upsilon u_{i,j} n_j\right) d\Gamma$$
$$+ \int_{\Omega} \tau u_k \phi_{\alpha,k}^e \left(u_j \phi_{B,j}^e u_{Bi} - \upsilon \phi_{B,jj}^e u_{Bi}\right) d\Omega + \int_{\Omega} \tau^b u_k u_j \phi_{\alpha,k}^e \phi_{B,j}^e u_{Bi} d\Omega$$
$$= 0$$

Assume that the Galerkin test function is linear, then the second derivative term vanishes. So that we have:

$$(B^e{}_{NM} + C^e{}_{NM}) u_{Bi} + K^e{}_{NM} u_{Bi} = C^e{}_N$$

Where:

$$B^e{}_{NM} = \int_{\Omega} \left(u_j \phi_\alpha^e \phi_{B,j}^e\right) d\Omega$$
$$K^e{}_{NM} = \int_{\Omega} \left(\upsilon \phi_{\alpha,j}^e \phi_{B,j}^e\right) d\Omega$$
$$C^e{}_{NM} = \int_{\Omega} (\tau + \tau^b) u_k u_j \phi_{\alpha,k}^e \phi_{B,j}^e d\Omega$$
$$C^e{}_N = \int_{\Gamma} \left(\phi_\alpha^* \upsilon u_{i,j} n_j\right) d\Gamma$$

As was showed above, the GPG is a mathematical method used to obtain approximate solutions of partial differential equations and numerical diffusions are added to stabilize the solutions. The method generates an equation system, where the number of term will depend of the number of nodes in each finite element.

The discretization of the three-dimensional solid-fluid domain has been developed using tetrahedral elements. Linear elements are used in the temperature and pressure field, which means 4 nodes by each elements. Moreover, quadratic elements (P2) are used in the velocity field, which means 10 nodes by each elements are considered for determining the velocity field.

$$T^e = \sum_{N=1}^{N} \phi_{N,L}^e * T_N^e \,;\; P^e = \sum_{N=1}^{N} \phi_{N;L}^e * P_N^e \;;\; u^e = \sum_{N=1}^{N} \phi_{N,Q}^e * u_N^e$$

$$\phi_{N;L}^e = Linear\ approximation;\;\; \phi_{N;Q}^e = Quadratic\ approximation$$

$$\sum_{N=1}^{N} \phi_N^e = 1\,;\; 0 \le \phi_N^e \le 1$$

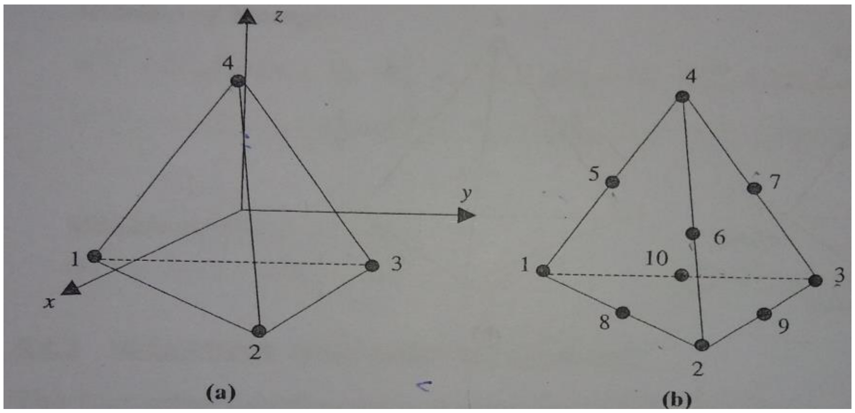

Figure-33: (a) Linear tetrahedral element, (b) Quadratic tetrahedral element.

The governing equations request a nonlinear solver. The nonlinear solver iterates to reach the final solution. In each iteration, the linearized version of the nonlinear system is solved using a linear solver. For conjugate heat transfer-laminar problems a segregate solver is used, the first solver is for the velocity and pressure field and the second one is used only by the temperature field. The damped Newton method is used as the nonlinear solver and the Pseudo time stepping method is invoked by improving the convergence in the solution of the Navier-Stoke equation, using the default parameters suggested by COMSOL-5.1 to the Courant number (CFL). On the other hand, the linearized version of the nonlinear system generated in CFD simulations consists in nonsymmetric matrices, therefore, the Generalized Minimal Residual algorithm (GMRES) is employed, which is an iterative method for the numerical solution of a nonsymmetric system of linear equations.